Quantification of Global Cloud Properties with Use of Spherical Harmonic Functions

Jiachen Ding[1*], Ping Yang[1], Lifan Wang[2], Elaine Oran[3], Norman G. Loeb[4], William L. Smith Jr.[4], Patrick Minnis[4,5]

[1]Department of Atmospheric Sciences, Texas A&M University, College Station, TX, USA.

[2]Department of Physics & Astronomy, Texas A&M University, College Station, TX, USA.

[3]Department of Aerospace Engineering, Texas A&M University, College Station, TX, USA.

[4]NASA Langley Research Center, Hampton, VA, USA

[5]Science Systems and Applications, Inc., Hampton, VA, USA

Corresponding author: Jiachen Ding (njudjc@tamu.edu)

Key Points:

- Spherical harmonic functions can be used to accurately depict global cloud properties.
- Degree 2 spherical harmonic component anomaly of cloud radiative effect is correlated with El Niño-Southern Oscillation.
- Degrees 3 to 8 spherical harmonic components of cloud radiative effect are correlated with Hadley Circulation.

Abstract

Spherical harmonic (SH) expansion is a useful tool to study any variable that has valid values at all latitudes and longitudes. The variable can be quantified as a sum of different spherical harmonic components, which are the spherical harmonic functions multiplied by their expansion coefficients. We find that the SH components of cloud radiative effect (CRE) have correlations with El Niño-Southern Oscillation (ENSO) and the Hadley Circulation (HC). In particular, the expansion degree 2 ($l = 2$) SH power spectrum component anomaly of CRE is strongly correlated with ENSO. The two dipole patterns appearing in the $l = 2$ SH component anomaly map can be reasonably explained by a known mechanism of ENSO's impact on cloud properties. The $l = 3$ and $l = 5$ SH power spectrum components are correlated with HC intensity, whereas the $l = 6$ and $l = 8$ components are correlated with HC latitudinal widths. In ENSO warm and cold phases, the HC-correlated SH components have opposite anomalies, which suggests the impact of ENSO on HC. This study illustrates that the SH expansion technique provides a different perspective to study the impacts of large-scale atmospheric circulation on global cloud properties and radiative effects.

Plain Language Summary

Clouds are a critical atmospheric constituent in regulating earth's energy budget (controlling the global temperature) by reflecting incident sunlight (a cooling effect), and emitting radiation to the ground (warming below clouds) and to space. The net warming or cooling effect of these factors is called the cloud radiative effect (CRE). The CRE varies with ordinary climate oscillations such as the well-known El Niño-Southern Oscillation (ENSO), and may amplify or partly suppress long-term global warming depending on whether cloud cover diminishes or increases. This study tests a way to summarize global cloud property variations, observed in great detail by satellites, in terms of various two-dimensional characteristic patterns defined by the spherical harmonic functions. For example, ENSO variations can be clearly observed in one of the characteristic patterns of CRE changes.

1 Introduction

The spherical harmonic (SH) expansion technique maps a variable on a spherical surface to its representation in the SH function space in terms of SH expansion coefficients. This technique, also known as the spectral transform method, has been employed in global atmospheric modeling efforts (Williamson, 2007), including numerical weather prediction and climate models. The spectral transform method expresses and solves dynamic equations in SH function space (e.g., Platzman, 1960; Eliasen et al., 1970; Orszag, 1970), which can be more numerically efficient than traditional global models formulated in the grid-point space. Many numerical techniques such as the fast SH transform (e.g., Suda & Takami, 2001; Wedi et al., 2013) have been developed to improve the efficiency of the spectrum transform method.

SH expansions and analyses are also widely used in geophysics to derive SH expansion coefficients of gravity and geopotential from discrete high-resolution measurements (e.g., Kaula, 1959; Nerem et al., 1995; Tapley et al., 2004). Specifically, the Gravity Recovery and Climate Experiment (GRACE) mission (Tapley et al., 2004) publishes satellite-measured gravity field data products in the form of SH expansion coefficients (Cheng et al., 2011, 2013).

SH expansion is an essential tool in cosmic microwave background (CMB) studies (e.g., Kamionkowski et al., 1997; Hu et al., 2001; Tegmark et al., 2001; Wang et al., 2002; Abramo &

Pereira, 2010). The magnitudes, positions, and shapes of power spectrum peaks of the CMB temperature fluctuation map are related to many cosmological parameters such as baryon density, dark matter density, and dark energy density. Thus, the variations of the cosmological parameters can be estimated from the power spectra derived from CMB observations.

Koppelt et al. (1989) show that the distribution of continents and oceans on the earth can be represented by SH expansion coefficients as low as 34 degrees. The coastlines interpreted from the reconstructed continent-ocean distributions are consistent with the actual coastline.

To date, although SH expansion has seen a few applications as noted above, we believe this method has been underutilized in research involving global datasets and can be successfully extended to additional global geophysical variables. In this study, we demonstrate the applicability of the SH expansion technique for representing cloud property data, such as cloud optical depth (COD), cloud fraction (CF), and cloud effective pressure (CEP) for evaluating global cloud radiative effects (CRE). We also explore how to interpret variations of individual SH expansion components of global cloud properties.

Ramanathan et al. (1989) and others (e.g., Hartmann et al., 1992; Trenberth et al., 2009; Stephens et al., 2012) showed that clouds are critical to the earth's radiative budget by reflecting and absorbing solar radiation, and absorbing and emitting terrestrial thermal radiative energy. Based on satellite remote sensing, clouds cover about 56% to 73% of the globe (Stubenrauch et al., 2013), depending on the definition of cloud coverage. Clouds and their physical properties have complex spatial and high-frequency temporal variations, but their global distribution and variations are closely related to large-scale atmospheric circulation including ENSO and HC.

Based on surface observations, Eastman et al. (2011) find that tropical cloud cover interannual variations are correlated with ENSO. ENSO can affect both low cloud (e.g., Park & Leovy, 2004; Zhu et al., 2007) and high cloud (e.g., Norris, 2005; Marchand, 2013) amounts via anomalous sea surface temperature and convection variations. Generally, low clouds have negative CRE (radiative cooling), and high clouds have positive CRE (radiative warming). The CRE is thus also affected by ENSO (e.g., Moore & Vonder Haar, 2001; Cess et al., 2001a, 2001b; Allan et al., 2002; Burleyson et al., 2015). The resulting cloud radiative heating variation can in turn modify cloud properties (Harrop & Hartmann, 2016). As the strongest atmospheric meridional circulation, the HC significantly affects cloud meridional distributions by varying their intensity, positions of ascending and descending branches, and cell widths. Previous studies (e.g., Oort & Yienger, 1996; Stachnik & Schumacher, 2011; Loeb et al., 2014) suggest substantial and complicated relationships between ENSO and HC anomalies and their impacts on global cloud properties and CRE.

In this study, we use SH expansion to investigate the impacts of ENSO and HC on CRE, which may provide a different perspective on the impact of atmospheric circulation on clouds and their radiative effects. Section 2 describes methods and data used in this study, including illustrating the accuracy of representing cloud properties using finite numbers of SH functions. Section 3 presents the results and discussions, and section 4 summarizes the main findings.

2 Methods and Data

2.1 Spherical harmonic expansion

The cloud properties considered in this study are COD (or τ), CF, CEP and CRE. Hereafter, CRE is defined as the net TOA radiative flux difference between cloudy and clear-sky conditions. Net radiative flux is computed as the difference between the downward flux and upward flux. Theoretically, a global cloud property can be expanded in an infinite number of SH functions. Practically, we can only expand cloud properties in terms of finite SH functions, and retain acceptable accuracy. For example, the global COD is expanded as

$$\tau(\theta,\varphi) = \sum_{l=0}^{\infty}\sum_{m=-l}^{m=l} C_{l,m}Y_{l,m}(\theta,\varphi), \quad (1)$$

where $Y_{l,m}(\theta,\varphi)$ is a SH function with degree l and order m, and θ and φ are zenith and azimuth angles (equivalent to latitude and longitude) at the surface of the earth. The expansion coefficients $C_{l,m}$ are computed by

$$C_{l,m} = \int_0^{2\pi}\int_0^{\pi} \tau(\theta,\varphi)Y_{l,m}^*(\theta,\varphi)\sin\theta d\theta d\varphi. \quad (2)$$

where the asterisk symbol denotes the complex conjugate. The cloud properties are discretized into latitude and longitude grids constructed using Hierarchical Equal Area isoLatitude Pixelization (HEALpix; https://healpix.sourceforge.net/) (Górski et al., 2005; Zonca et al., 2019), which facilitates a fast discrete SH transform using an open-source software package available on the web page.

With the truncation of the coefficient series $C_{l,m}$ to degree L, a finite series of SH terms can be used to reconstruct the global COD distribution in the form

$$\tau_L(\theta,\varphi) = \sum_{l=0}^{L}\sum_{m=-l}^{m=l} C_{l,m}Y_{l,m}(\theta,\varphi). \quad (3)$$

Because the cloud properties involved in this study are mathematically real quantities, the SH expansion coefficients satisfy $C_{l,m} = C_{l,-m}$. The number of independent coefficients N from degree 0 to L is

$$N = \frac{L(L+1)}{2} + L + 1. \quad (4)$$

Each cloud property SH expansion is evaluated by comparing CRE computations using the original COD data (e.g., τ) and reconstructed data (e.g., τ_L).

To evaluate the contribution of SH expansion components of individual degrees, the SH power spectrum p_l^{SH} is defined as

$$p_l^{\mathrm{SH}} \equiv \frac{1}{2l+1}\sum_{m=-l}^{l} C_{l,m}C_{l,m}^*. \quad (5)$$

According to the SH addition theorem and Eq. (2), for $\tau(\theta,\varphi)$, we have

$$p_l^{\mathrm{SH}} = \frac{1}{4\pi}\int\int P_l(\hat{r}\cdot\hat{r}')\tau(\hat{r})\,\tau(\hat{r}')d\Omega d\Omega', \quad (6)$$

where P_l is the Legendre polynomial of degree l, $\hat{r}$ is a unit vector corresponding to the angular coordinates θ and φ, and Ω is the solid angle. $\hat{r}'$ and Ω' are defined in the same manner. Equation (6) suggests that p_l^{SH} measures the prevalence of cloud spatial variations with a specific angular separation consistent with the widths of P_l peaks which are roughly equal to $\Delta\Theta =$

$180°/l$. The SH power spectrum of clouds can be used to analyze the variation of cloud spatial distributions of specific scales.

2.2 Cloud radiative effect computation

The differences between computed CRE with original and reconstructed cloud properties are used to evaluate the accuracy of the SH expansion of selected cloud properties. In particular, the net radiative flux at the TOA is computed by using the Rapid Radiative Transfer Model for general circulation model applications (RRTMG) (Clough et al., 2005; Iacono et al., 2008), in which SW and LW components are treated separately by RRTMG_SW and RRTMG_LW.

The global COD, CF, and CEP data in the RRTMG computation are obtained from the CERES Energy Balanced and Filled (EBAF) dataset (Loeb et al., 2018a; Kato et al., 2018). The CERES EBAF dataset contains monthly-averaged global longwave and shortwave flux as well as CRE data at both the top of the atmosphere (TOA) and the surface with 1° spatial resolution. The single-layer monthly-averaged COD, CF and CEP data are available in EBAF and are used in a radiative transfer model to compute CRE. The CF and CEP data cover both day and night, while COD data are only available for daytime.

The monthly-averaged COD, CF and CEP data from the CERES EBAF dataset are the inputs to RRTMG. The fractions of liquid and ice clouds are estimated from the cloud water content data of the European Centre for Medium Range Weather Forecasts (ECMWF) Reanalysis 5th Generation (ERA5) global reanalysis dataset (Hersbach et al., 2020). The global-averaged cloud effective radius (CER) from the MODIS Collection 6 cloud product (Platnick et al., 2017) is 32 μm for ice clouds and 12 μm for liquid clouds (Yi et al., 2017). For simplicity, we use the above-mentioned global-averaged CER at all locations. The COD data are given in a visible spectral band. By assuming the extinction efficiency in a visible band to be 2, the COD data can be converted to liquid water path (LWP) and ice water path (IWP). LWP and IWP can be used to obtain CODs in different RRTMG bands together with the CER values.

The liquid water cloud optical properties assumed in the MODIS Collection 6 cloud property retrievals (Platnick et al., 2017) are parameterized and used in RRTMG computations. The two-habit ice cloud optical property model (Loeb et al., 2018b) is parameterized and used in RRTMG computations involving ice clouds. The cloud layers are assumed to follow the maximum-random overlap with the Monte Carlo Independent Column Approximation (Pincus et al., 2003). All clouds are single-layered and homogeneous in the computation. The RRTMG computations in longwave bands explicitly consider cloud multiple scattering effects. Previous studies (e.g., Kuo et al., 2017; Gu et al., 2021) have shown the significance of accounting for cloud multiple scattering in longwave radiative flux computations. The 2/4-stream approximation method (Toon et al., 1989; Fu et al., 1997; Kuo et al., 2020) is incorporated into the RRTMG_LW runs to account for cloud multiple scattering.

Other input data are averaged over the month to be consistent with the cloud property data. The atmospheric profile data including temperature, water vapor concentration, and ozone concentration are from the ERA5 global reanalysis data mentioned above. Concentrations of absorptive gases CO_2, CH_4, and CO are taken from the Copernicus Atmosphere Monitoring Services (CAMS) reanalysis of atmospheric composition (Inness et al., 2019). The present RRTMG_SW and RRTMG_LW runs use ERA5 monthly averaged surface albedos and surface emissivities for different surface types from ECMWF (2020), respectively. Solar zenith angles

are specified to be monthly averaged values computed according to Gupta et al. (2001). Aerosols are not considered in the present RRTMG runs.

2.3 El Niño-Southern Oscillation index and Hadley Circulation parameters

We consider the impact of ENSO and HC on CRE. The CRE data are derived from the CERES EBAF dataset from the year 2000 to 2021. The overlapping bi-monthly Multivariate ENSO Index (MEI) (Wolter & Timlin, 1998, 2011) time series are used to quantify the ENSO. The HCs are characterized by the zonal-mean meridional streamfunction (ψ), which is computed using the meridional wind field from ERA5 global reanalysis data. ψ is a function of pressure p and latitude θ, and is calculated as (Nguyen et al., 2013)

$$\psi(p,\theta) = \frac{2\pi R_e \cos\theta}{g} \int_p^{p_s} \bar{v}(p,\theta)dp, \quad (7)$$

where R_e is the averaged radius of the earth, g is the gravitational acceleration, p_s is the surface pressure and $\bar{v}(p,\theta)$ is the zonal-mean meridional wind at pressure level p and latitude θ.

The HC parameters include HC intensity and latitudinal widths. The HC intensity is defined as the maximum absolute value of the streamfunction $\psi_{\max}$. The edges of HC cells are denoted by the latitudes of ψ zero isolines averaged between pressure level 400 hPa and 600 hPa (Nguyen et al., 2013). The edge closest to the equator is defined as the intersection between the northern and southern HC cells. The latitudinal width of an HC cell is defined as the latitudinal difference between its poleward edge and the intersection.

3 Results

3.1 Evaluation of cloud property spherical harmonic expansion

Figure 1 shows the differences between the original and reconstructed net CRE and COD global distributions, defined as $\Delta F_{CRE,L}(\theta,\varphi) = F_{CRE,L}(\theta,\varphi) - F_{CRE}(\theta,\varphi)$ and $\Delta\tau_L(\theta,\varphi) = \tau_L(\theta,\varphi) - \tau(\theta,\varphi)$, for L equal to 100 and 200, which correspond to 5151 and 20301 coefficients, respectively. Net CRE is the sum of shortwave (SW) and longwave (LW) CRE. Obviously, with a larger L, $\Delta F_{CRE,L}(\theta,\varphi)$ and $\Delta\tau_L(\theta,\varphi)$ decrease globally. The normalized distribution density plots in Figs. 1d and 1h show errors almost equally distributed around 0. The root-mean-square errors (RMSEs) of reconstructed CRE are 4.15 and 2.01 W m^{-2}, and the RMSEs of reconstructed COD are 0.45 and 0.22 for L equal to 100 and 200, respectively. For $L = 200$, the standard deviation of $\Delta\tau_L$ is estimated to be 0.22. Because the global mean $\Delta\tau_L$ is almost zero, the value of the standard deviation is very close to the RMSE of the reconstructed COD. This suggests that about 95% of $\Delta\tau_L$ values are less than 0.44, so the global COD data can be represented by 20301 SH expansion coefficients with high accuracy. The global CRE, CF, CEP and radiative flux data can also be accurately represented in the same manner with a limited number of coefficients.

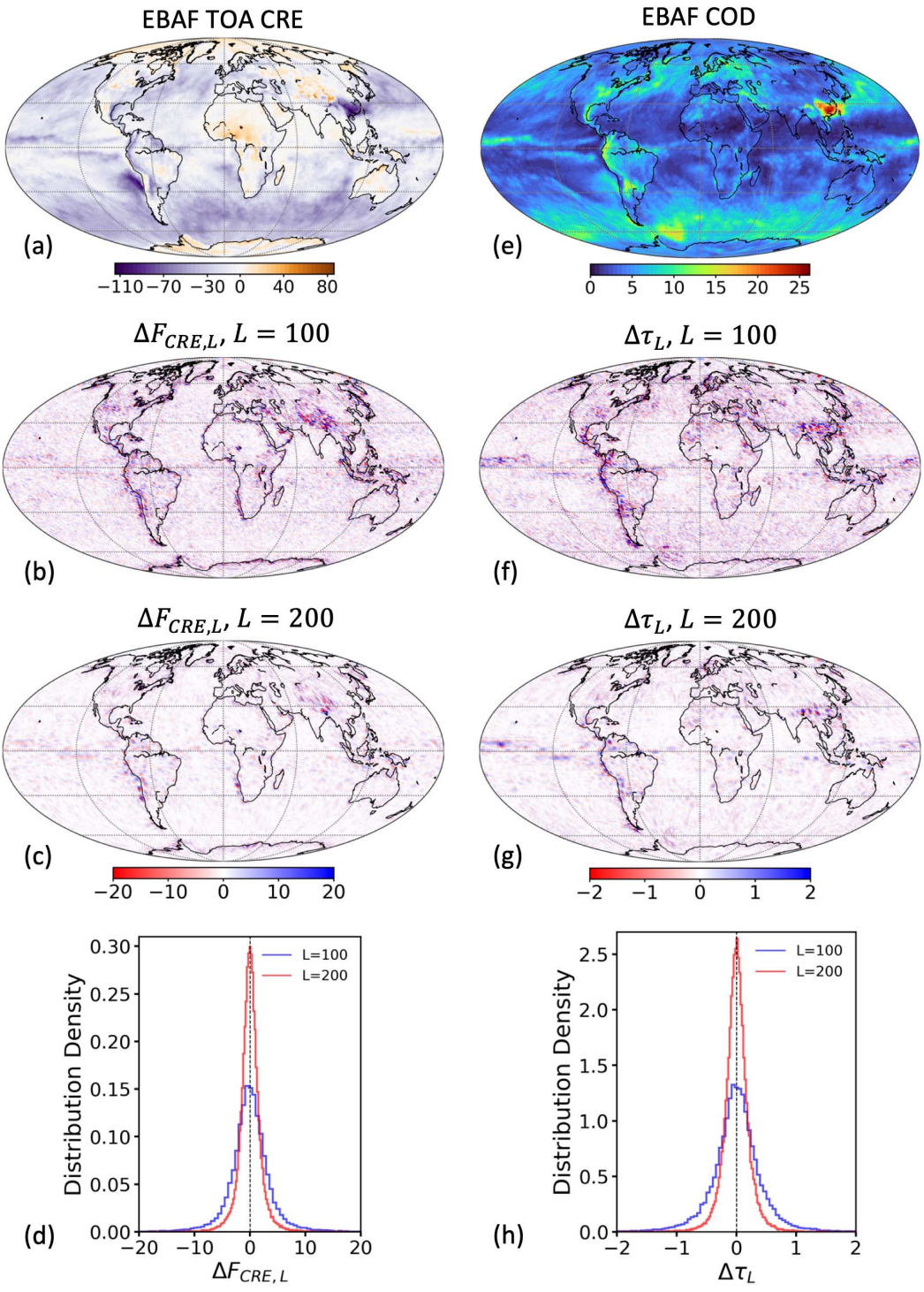


Figure 1. (**a**): March 2019 monthly-averaged net (SW+LW) TOA CRE derived from CERES EBAF dataset; (**b**)-(**c**): Spatial patterns of the difference between CRE in (**a**) and the reconstructed counterpart, defined as $\Delta F_{CRE,L}(\theta,\varphi)$ in the text, with 100 and 200 degrees of SH functions; (**d**): normalized distribution density (the area under each curve is equal to 1) of $\Delta F_{CRE,L}(\theta,\varphi)$ in (**b**) and (**c**); (**e**): March 2019 monthly-averaged COD derived from CERES EBAF dataset; (**f**)-(**g**): Spatial patterns of the difference between COD in (**e**) and the

reconstructed counterpart, defined as $\Delta\tau_L(\theta,\varphi)$ in the text, with 100 and 200 degrees of SH functions; (**h**): normalized distribution density of $\Delta\tau_L(\theta,\varphi)$ in (**f**) and (**g**).

Figure 2 shows the annual mean CRE computed with the CERES EBAF cloud properties including COD, CF and CEP, and the CRE difference ($\Delta F_{CRE,L}$) between CRE computed with original (F_{CRE}) and reconstructed ($F_{CRE,L}$) cloud properties, where subscript L indicates the maximum SH expansion degree. As shown in the CRE difference plots in Fig. 2, the errors of $F_{CRE,100}$ are noticeable in regions with strong CRE such as the Intertropical Convergence Zone (ITCZ) and coastal region of the South America. For $L = 100$, the RMSE of SW and LW CRE errors are 2.18 and 0.85 W m^{-2}. If $L = 200$, the global $\Delta F_{CRE,L}$ is significantly reduced, and the standard deviation of SW and LW CRE errors are 1.24 and 0.60 W m^{-2}. For about 95% of the pixels, the SW and LW CRE errors are less than 2.48 and 1.20 W m^{-2}. The normalized distribution density of positive and negative $\Delta F_{CRE,L}$ is symmetric with respect to the zero line, as indicated by Figs. 2g and 2h for both SW and LW CRE.

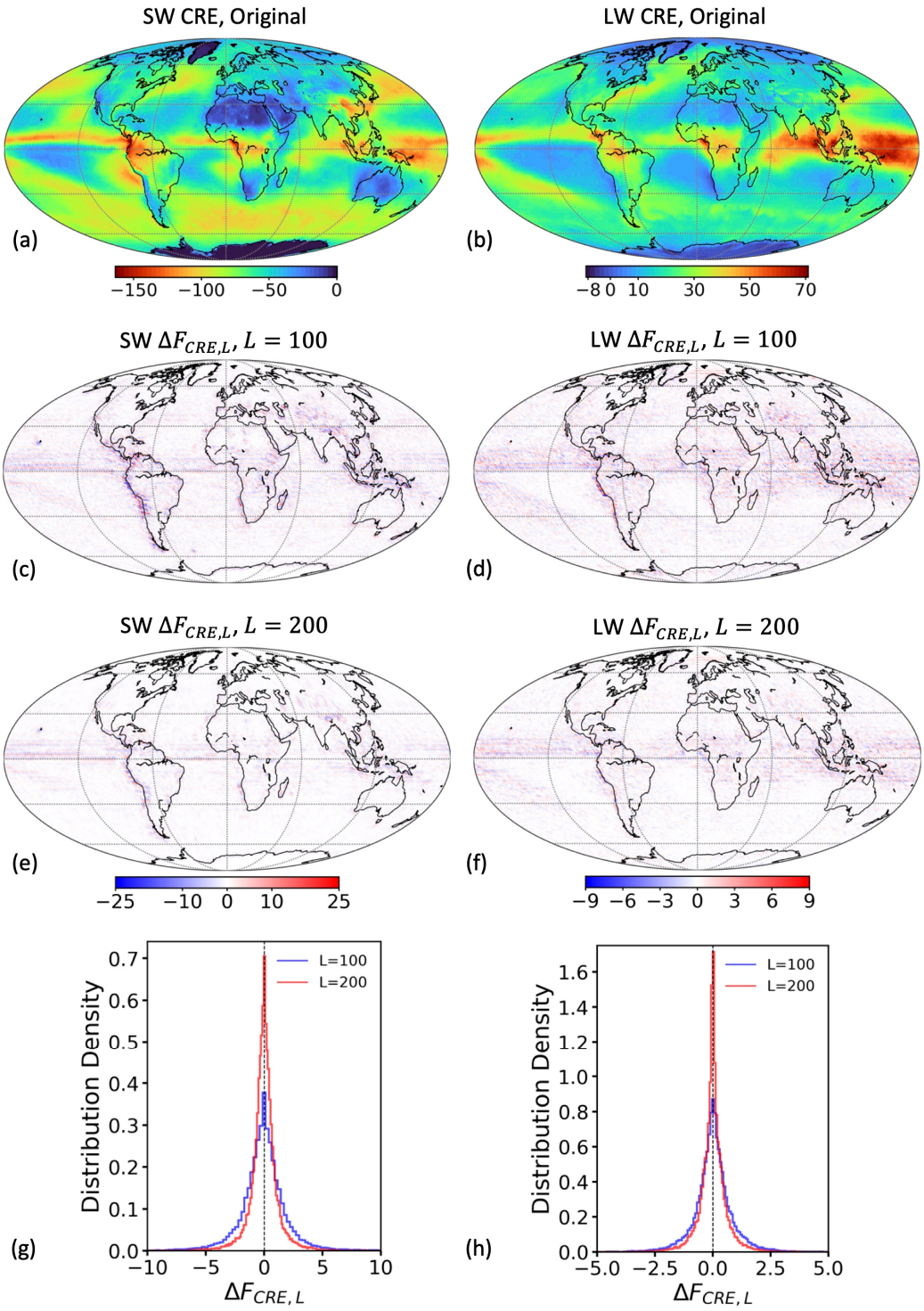


Figure 2. **(a)-(b)**: 2019 annual mean SW and LW CRE (W m^{-2}) computed by RRTMG with original CERES EBAF cloud properties including COD, CF and CEP; **(c)-(f)**: CRE difference ($\Delta F_{CRE,L}$) between CRE computed with original and reconstructed cloud properties. **(c)-(d)**: SW and LW $\Delta F_{CRE,L}$ with $L = 100$; **(e)-(f)**: SW and LW $\Delta F_{CRE,L}$ with $L = 200$; **(g)**: normalized distribution density of SW $\Delta F_{CRE,L}$ in **(c)** and **(e)**; **(h)**: normalized distribution density of LW $\Delta F_{CRE,L}$ in **(d)** and **(f)**.

247

248 3.2 Spherical harmonic power spectra

249 Figure 3(a-c) shows the SH power spectra (p_l^{SH}) of annual mean SW, LW and net CRE
250 from 2001 to 2020 (Note that each panel in Fig. 3 contains 20 curves). The CRE data are from
251 the CERES EBAF dataset. Over the 20 years, the positions of the spectral peaks are consistent.
252 The SW CRE power spectra have strong peaks at $l = 4$ and $l = 6$, the LW CRE power spectra
253 have strong peaks at $l = 2$ and $l = 6$, and the net CRE power spectra have strong peaks at $l = 4$
254 and $l = 6$. $l = 2$, $l = 4$, and $l = 6$ correspond to angular scales 90°, 45° and 30°, as explained in
255 Section 2.1. As shown in Fig. 3(d-f), the latitudinal variations of the zonally averaged annual
256 mean CRE ($\bar{F}_{CRE}$) have peaks with widths of roughly 45° and 30°. The hemispheric symmetry is
257 also obvious, which corresponds to a latitudinal variation of 90°. We then apply the one-
258 dimensional Fourier transform to the zonally averaged annual mean CRE, and show the Fourier
259 transform power spectra ($|f(\bar{F}_{CRE})|^2$) in Fig. 3(g-i). Different Fourier transform spectral
260 components have different latitudinal variation periods. A half of the latitudinal variation period
261 is the width of the peak of latitudinal variation. At half periods 90°, 45° and 30°, Fig. 3(g-i)
262 show that the SW, LW and net CRE $|f(\bar{F}_{CRE})|^2$ are the largest at 45°, 90° and 45°, respectively.
263 This is consistent with the strongest p_l^{SH} peaks at $l = 4$ for SW, at $l = 2$ for LW, and at $l = 4$ for
264 net CRE, as shown in Fig. 3(a-c). In addition, the local maxima of LW CRE $|f(\bar{F}_{CRE})|^2$ at half
265 period 30° is consistent with the local maxima of LW CRE p_l^{SH} at $l = 6$. The above analysis
266 suggests that the CRE SH power spectrum is associated with the latitudinal variation of CRE.
267 According to Eq. (6), the SH power spectrum also accounts for variations that are not along the
268 latitudinal direction.

269 Figures 4a and 4b show the SH power spectra of annual mean low and midlevel (>450
270 hPa), and high (<450 hPa) cloud water path (CWP) from 2001 to 2020. The power spectrum
271 curves of the low and midlevel cloud CWP and high cloud CWP resemble those of the SW CRE
272 and LW CRE, respectively. The similarity in the SH power spectrum curve shapes indicates
273 similarity in spatial distribution. The SW CRE spatial distribution is more relevant to the low and
274 midlevel cloud, and the LW CRE spatial distribution is more relevent to the high cloud. The SW
275 CRE results from clouds reflecting incident solar radiation. Global low clouds greatly modify the
276 albedo of the earth, and their reflecting effect (radiative cooling) dominates their thermal
277 emission effect toward the surface (radiative warming) (Hartmann et al., 1992). In LW, clouds
278 absorb thermal emission from the atmosphere and emit LW radiation to space at a lower
279 temperature than the surface. High clouds, which usually have a lower cloud top temperature,
280 contribute more to LW CRE than low clouds. The SW CRE (Fig. 3a), net CRE (Fig. 3c) and
281 low-midlevel cloud (Fig. 4a) SH power spectra all have strong peaks at $l = 4$, which implies the
282 significant SW CRE contribution to net CRE by low-midlevel clouds.

283 One interesting feature in the CRE and CWP SH power spectra (Figs. 3 and 4) is that the
284 power spectrum components at even degree l is systematically stronger than at odd l. This can be
285 explained by the symmetry of clouds in the northern and southern hemispheres. The Legendre
286 polynomial P_l is even at even l and is odd at odd l. According to Eq. (6), at an odd l, if $\tau(\hat{r}) = \tau(-\hat{r})$, the values $\tau(\hat{r})\tau(\hat{r}')P_l(\hat{r}\cdot\hat{r}')$ and $\tau(-\hat{r})\tau(\hat{r}')P_l(-\hat{r}\cdot\hat{r}')$ will cancel out in the
287 integration calculation. Therefore, if the cloud is symmetric to some extent with respect to the
288 equator, which can be seen in the zonally averaged CRE in Fig. 3, the SH power spectrum
289 components at odd l tend to be smaller than at even l.
290

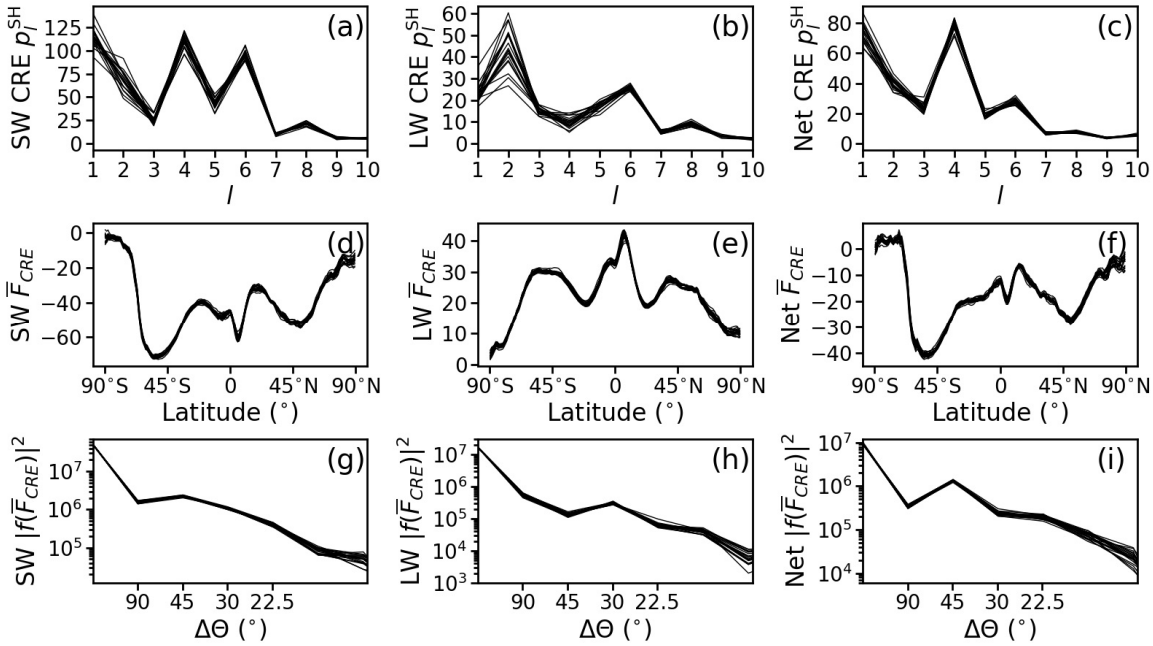


Figure 3. Quantities related to annual mean CRE between 2001 and 2020. (**a**-**c**): SW, LW and net (SW+LW) CRE SH power spectra p_l^{SH} with units of $\mathrm{W^2\ m^{-4}}$. The x-axis is the SH degree l. (**d**-**f**): Zonally averaged SW, LW and net CRE ($\bar{F}_{CRE}$) at different latitudes, with units of $\mathrm{W\ m^{-2}}$. (**g**-**i**): Fourier transform power spectra of zonally averaged CRE ($|f(\bar{F}_{CRE})|^2$), with units of $\mathrm{W^2\ m^{-4}}$. The x-axis is the half period of the corresponding spectral component.

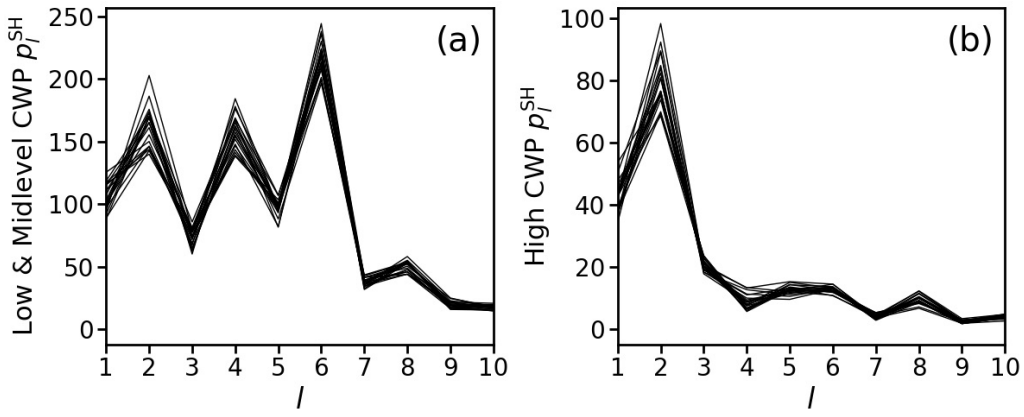


Figure 4. SH power spectra p_l^{SH} of annual mean low and midlevel (**a**), and high (**b**) cloud water path (CWP) between 2001 and 2020. The CWP data are derived from the ERA5 dataset. The x-axis is the SH degree l. The CWP SH power spectra have units of $\mathrm{g^2\ m^{-4}}$.

3.3 Impact of El Niño-Southern Oscillation on cloud radiative effect

Figure 5 shows the correlation coefficients (r) between MEI and anomalies of CRE p_l^{SH} (Δp_l^{SH}) at various expansion degrees. To be consistent with the bi-monthly MEI, the CRE p_l^{SH} are computed using bi-monthly averaged global CRE data from the CERES EBAF dataset

spanning from March 2000 to December 2021. The anomaly of a p_l^{SH} is the difference between the bi-monthly p_l^{SH} for a specific two months in a given year and the averaged bi-monthly p_l^{SH} for the same two months in all available years. As a comparison, the dotted lines in Fig. 5 also show r between MEI and the anomalies of global mean bi-monthly averaged SW, LW and net CRE ($\Delta\bar{\bar{F}}_{CRE}$). The correlations between MEI and $\Delta\bar{\bar{F}}_{CRE}$ are weak for SW, LW and net CRE, with r values 0.213, –0.057 and 0.202 repectively. Because SW CRE dominates globally over LW CRE, r for net $\Delta\bar{\bar{F}}_{CRE}$ is similar to SW $\Delta\bar{\bar{F}}_{CRE}$.

Because r for CRE Δp_l^{SH} varies substantially at different expansion degrees, it is evident that ENSO has different impacts on different SH expansion components. At $l = 2$, the LW and SW CRE Δp_l^{SH} have relatively large correlations with MEI with r values –0.643 and –0.687. At $l = 2$, the correlation between net CRE Δp_l^{SH} and MEI is much weaker than for the SW and LW counterparts. ENSO affects the SH expansion components of SW and LW CRE in opposite directions, so the impact on the net CRE is insignificant.

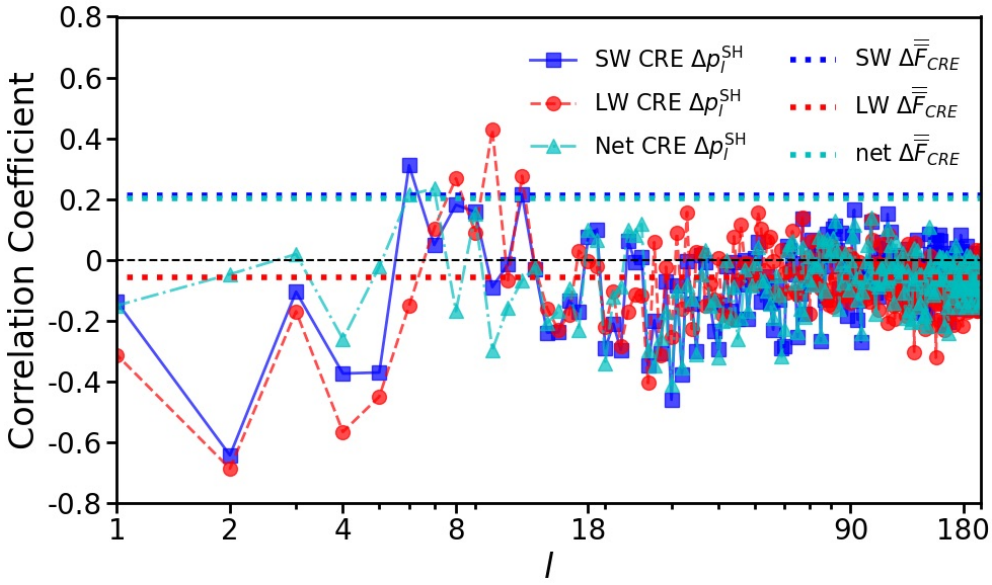


Figure 5. The correlation coefficients between anomalies of CRE SH power spectrum components (Δp_l^{SH}) and MEI. The CRE SH power spectra are computed using bi-monthly averaged global CRE data from the CERES EBAF dataset. The data span from March 2000 to December 2021. The anomaly of a power spectrum is the difference between the bi-monthly power spectrum for specific two months at a given year and the averaged bi-monthly power spectrum for the two months at all available years. The blue square, red circle and cyan triangle symbols are for SW, LW and net CRE, respectively. The blue, red and cyan dotted lines show the correlation coefficients between MEI and anomalies of global mean bi-monthly averaged SW, LW and net CRE ($\Delta\bar{\bar{F}}_{CRE}$), respectively.

Figure 6 shows the time series of the MEI plotted together with global mean CRE anomalies $\Delta\bar{\bar{F}}_{CRE}$ and CRE Δp_2^{SH}. In some strong El Niño years such as 2015-2016 and La Niña

years such as 2010-2011, the global mean SW CRE anomalies are strongly correlated with the MEI, but the correlation is not obvious in other years. The correlation between global mean LW CRE anomalies and the MEI is weak in all the considered years. In contrast, the LW and SW CRE Δp_2^{SH} have strong correlation with the MEI in all the considered years. MEI ≥ 0.5 corresponds to an ENSO warm phase (El Niño-like), MEI ≤ –0.5 corresponds to an ENSO cold phase (La Niña-like), and –0.5 < MEI < 0.5 is an ENSO neutral phase (Zhang et al., 2019). In most of the considered years, a positive (negative) MEI corresponds to a negative (positive) Δp_2^{SH} for both SW and LW CRE. In the ENSO warm (cold) phase, the contribution of the $l = 2$ SH component decreases (increases) relative to the neutral phase for both SW and LW CRE.

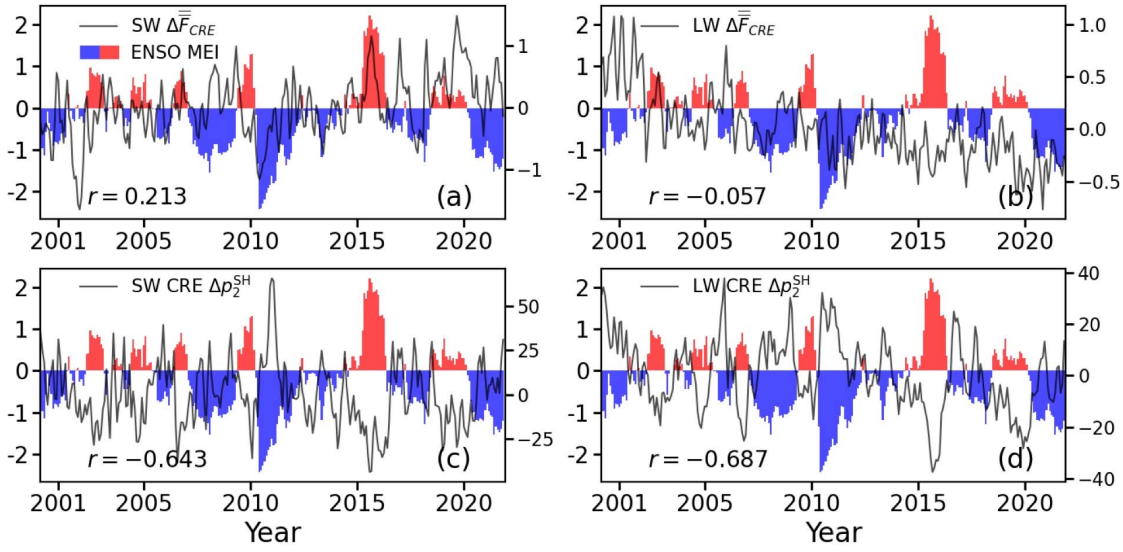


Figure 6. Time series of MEI plotted together with the anomalies of CRE-related quantities. In each panel, the left axis shows the MEI, and the right axis is the scale for CRE-related quantities. The bars of positive and negative MEI values are filled with red and blue colors. Panels (**a**) and (**b**) show global mean bi-monthly averaged CRE anomalies ($\Delta\bar{\bar{F}}_{CRE}$). Panels (**c**) and (**d**) show the anomalies of CRE SH power spectrum components at $l = 2$ (Δp_2^{SH}). (**a**) and (**c**): SW; (**b**) and (**d**): LW. CRE units are W m^{-2}, and SH power spectra units are W^2 m^{-4}. The correlation coefficients (r) of MEI and the CRE-related anomalies are denoted in each panel.

A degree l SH component is defined as

$$x_l(\theta,\varphi) = \sum_{m=-l}^{m=l} C_{l,m}^{x} Y_{l,m}(\theta,\varphi), \tag{8}$$

where x is a variable that has a valid value at each arbitrary latitude and longitude, x_l is the degree l SH component, and $C_{l,m}^{x}$ $(m = -l, -l+1, \ldots, 0, \ldots, l-1, l)$ are SH expansion coefficients of x at l. Figures 7a (7c) and 7b (7d) show the mean anomalies of the $l = 2$ SH component of SW (LW) CRE in ENSO warm and cold phases. The anomalies of the SH component in ENSO warm or cold phases are the mean anomalies over months with MEI ≥0.5 or ≤–0.5 respectively. The CRE data are bi-monthly averaged to be consistent with the MEI data. The anomaly of an SH component is the difference between the bi-monthly SH component for

any specific two months in a given year and the averaged bi-monthly SH component for the same two months in all available years.

As shown in Fig. 7, the mean anomalies of the $l = 2$ CRE SH component have a dipole pattern over the Indian and Pacific oceans. In the ENSO warm phase, the LW (SW) CRE dipole pattern is negative (positive) over Indonesia and the western Pacific, and positive (negative) over the central and eastern Pacific. In the ENSO cold phase, the dipole pattern is reversed and the magnitude is weaker than the warm phase. The variation of the dipole pattern is consistent with previous studies on the impact of ENSO on clouds over the tropics. In the ENSO warm phase, the low cloud fraction increases over Indonesia and decreases in the eastern Pacific (Zhu et al., 2007), whereas the high cloud fraction decreases over Indonesia and the western tropical Pacific, and increases over the central tropical Pacific (Norris, 2005; Marchand, 2013). The dipole patterns of SW and LW CRE have opposite signs over the Indian and Pacific oceans. Climatologically, the SW CRE value is negative (radiative cooling) and the LW CRE value is positive (radiative warming) in the dipole region. Although SW and LW CRE have different sensitivities to low and high clouds, the overall ability of cloud reflecting incoming solar radiation and reducing outgoing longwave emission is weakened (strengthened) over Indonesia and the western tropical Pacific, and is strengthened (weakened) over central and eastern tropical Pacific in the ENSO warm (cold) phase.

In Fig. 7, there is another dipole pattern centered over South America and Africa. In the ENSO warm phase, the SW (LW) CRE anomaly dipole pattern is negative (positive) over Africa, and positive (negative) over South America. In the ENSO cold phase, the dipole pattern is reversed and the magnitude is weaker than the warm phase. A modeling study by Yang et al. (2016) calculates the correlation coefficient between CRE and the Niño 3.4 index. The SW (LW) CRE over Africa have weak negative (positive) correlations with the Niño 3.4 index, and the signs of correlations are largely reversed over South America. This is consistent with the dipole pattern of the $l = 2$ CRE SH component anomalies over Africa and South America.

The above results and analysis indicate that the CRE Δp_2^{SH} can be an alternative parameter to measure the phase and strength of ENSO. The impact of ENSO on CRE is clearly present in the $l = 2$ CRE SH component anomalies.

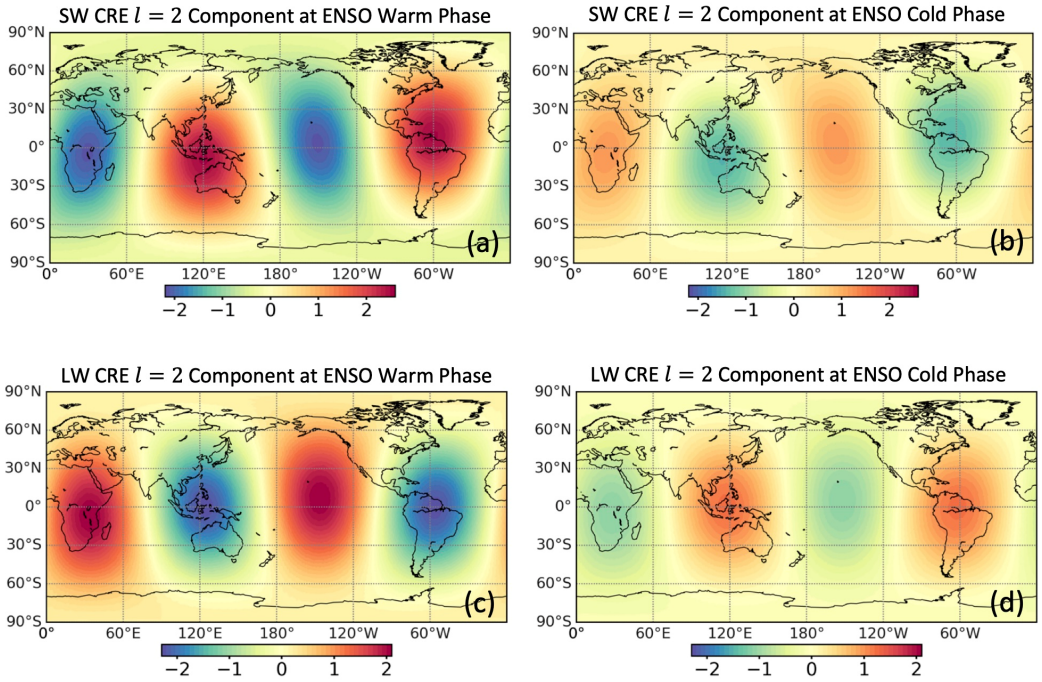


Figure 7. The mean anomalies of SH components at $l = 2$ of SW (**a**-**b**) and LW (**c**-**d**) CRE in ENSO warm (**a** and **c**) and cold (**b** and **d**) phases.

3.4 Impact of Hadley Circulation on cloud radiative effects

Figure 8 shows the r values between the monthly averaged HC parameters and LW CRE p_l^{SH} at various expansion degrees. The SW CRE p_l^{SH} has similar but weaker correlations with the HC parameters. At expansion degrees $l \leq 8$, p_l^{SH} is strongly correlated with HC intensity and width. In particular, r between p_l^{SH} of odd degrees and HC intensity is up to 0.767. The absolute value of r between p_l^{SH} of even degrees, and the northern and southern branch widths can be more than 0.8. r values are positive for the northern branch width and negative for the southern branch width.

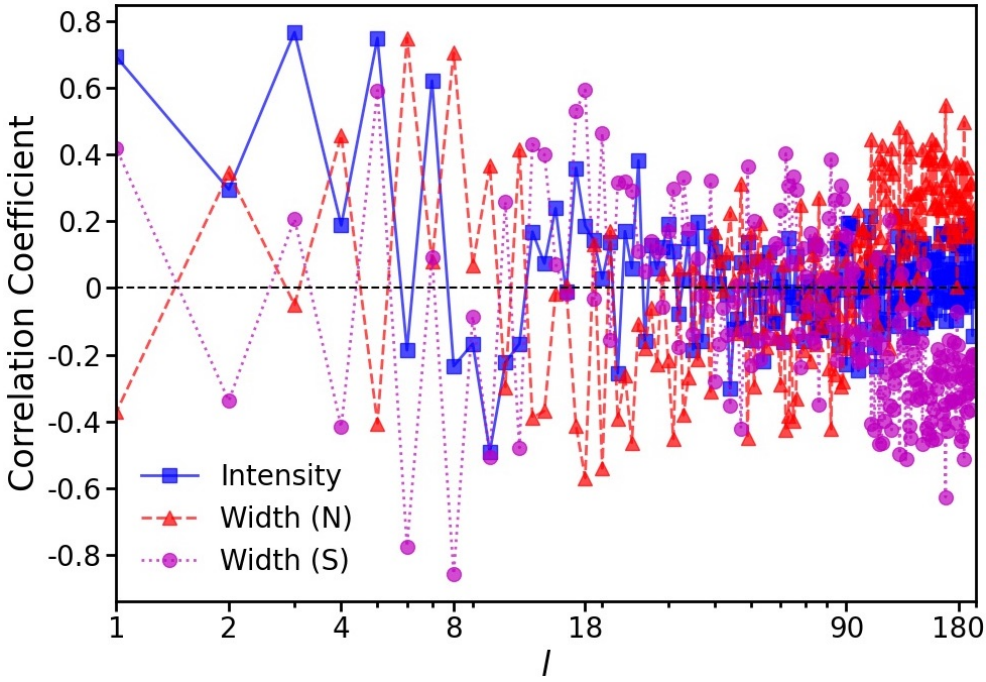


Figure 8. The correlation coefficients between LW CRE p_l^{SH}, and HC intensity (blue square symbols), or northern (red diamond symbols) or southern (magenta circle symbols) branch widths. The LW CRE SH power spectra are computed using monthly averaged global CRE data from the CERES EBAF dataset. The data span from January 2001 to December 2020. The definitions of the HC parameters are described in section 2.3.

Figure 9 shows the time series of the HC parameters plotted together with LW CRE p_l^{SH}. The variations of p_3^{SH} and p_5^{SH} are consistent with the HC intensity in most months. The oscillation of p_6^{SH} and p_8^{SH} time series is in phase with the northern branch width, and is in the opposite direction from the southern branch width. Now it is clear that the peaks at $l = 6$ and $l = 8$ in the CRE SH power spectrum (Fig. 3) are associated with the widths of HC branches.

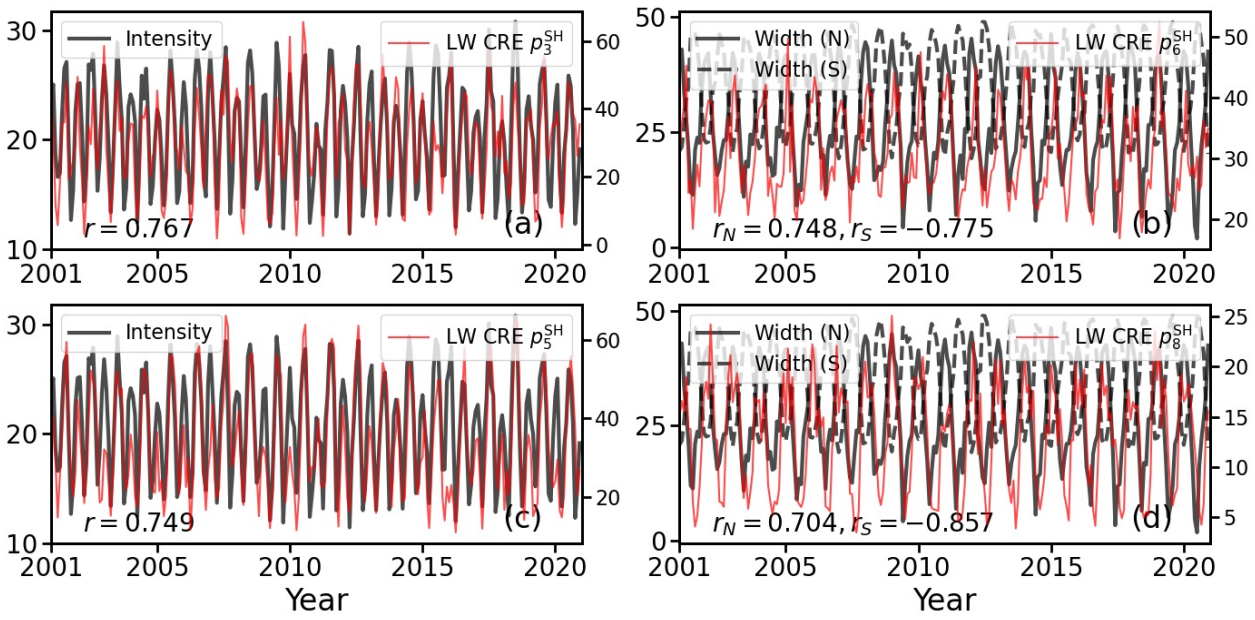


Figure 9. Time series of HC parameters plotted together with the LW CRE SH power spectrum component p_l^{SH}. For each panel, the left axis shows HC parameters, and the right axis shows p_l^{SH}. (**a**) and (**c**): The HC parameter is HC intensity scaled by 10^{-10} with units of kg s^{-1}. (**b**) and (**d**): The HC parameters are northern and southern branch widths with units of degrees of latitude (°). (**a**): LW CRE p_3^{SH}; (**b**): LW CRE p_6^{SH}; (**c**): LW CRE p_5^{SH}; (**d**): LW CRE p_8^{SH}. The CRE data have units of W m^{-2}, and the SH power spectra have units of W^2 m^{-4}. The correlation coefficients (r) of the HC parameters and p_l^{SH} are denoted in each panel. In panels (**b**) and (**d**), r_N and r_s are the correlation coefficients between p_l^{SH} and the northern and southern branch widths, respectively.

Using upper-air wind data, Oort and Yienger (1996) observed the correlation between ENSO and HC. The impact of ENSO on HC is also revealed in various reanalysis datasets (Stachnik & Schumacher, 2011; Nguyen et al., 2013). ENSO can cause strengthening and weakening of the local HC (Klein et al., 1999). Figure 10 shows the mean anomalies of the $l = 3$ and $l = 6$ LW CRE SH components in ENSO warm and cold phases. The signs of the SH component anomalies in ENSO warm and cold phases are opposite. Because the $l = 3$ and $l = 6$ components are strongly correlated with HC as shown in Fig. 9, ENSO's impact on the HC can be observed in the anomalous SH components in different ENSO phases. For example, in Figs. 10a and 10c, the LW CRE has positive anomalies over the equatorial central and eastern Pacific in the ENSO warm phase, which corresponds to increased cloud cover in those regions and indicates an enhanced local HC ascending branch. Klein et al. (1999) also found an enhanced HC in those regions during El Niño periods using upper-tropospheric relative humidity data.

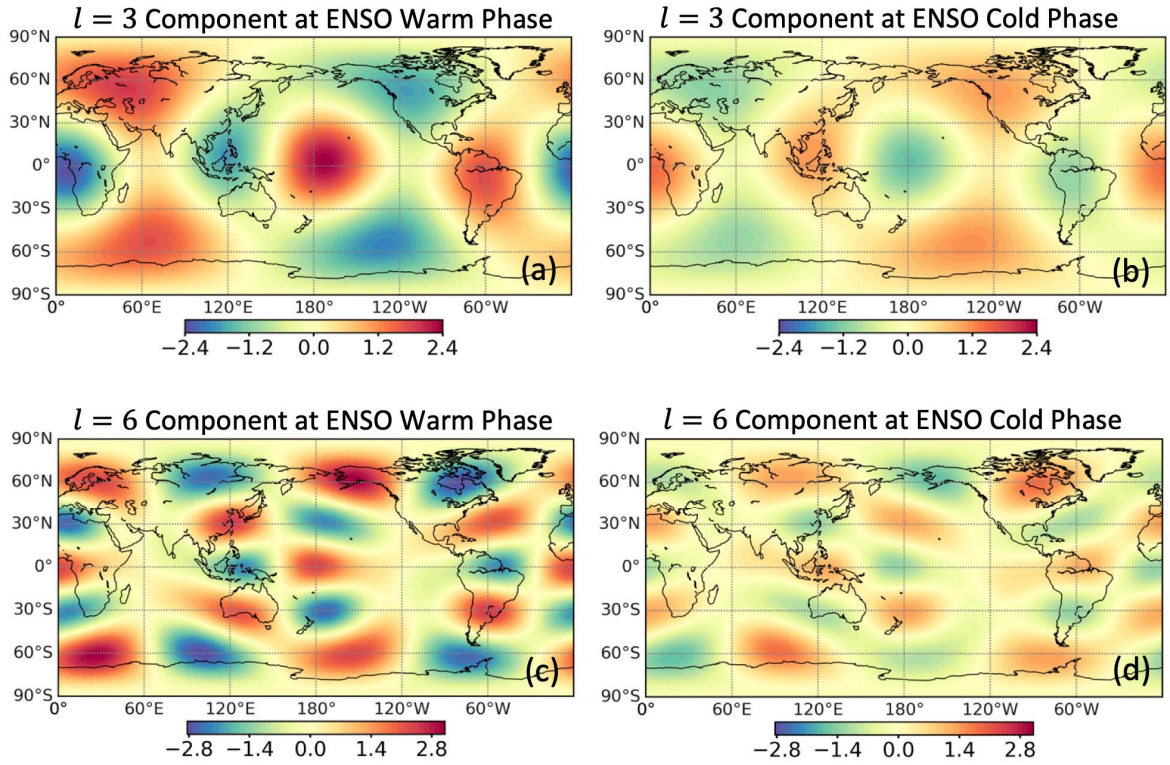


Figure 10. The mean anomalies of SH components at $l = 3$ (**a**-**b**) and $l = 6$ (**c**-**d**) of LW CRE in ENSO warm (**a** and **c**) and cold (**b** and **d**) phases.

4 Conclusions

The spherical harmonic (SH) expansion technique can quantify any variable which has valid values at each latitude and longitude in terms of different SH components. In this study, we investigate the impact of large-scale atmospheric circulation, including El Niño-Southern Oscillation (ENSO) and Hadley Circulation (HC), on SH components of global cloud radiative effect (CRE). This provides a different perspective about the impact of ENSO and HC on cloud properties and radiative effects.

We first validate the accuracy of using SH functions to represent global cloud properties, including cloud optical depth (COD), cloud fraction (CF), and cloud effective pressure (CEP). The accuracy of using a limited number of SH functions to represent COD, CF and CEP is evaluated concerning CRE computation. Based on year 2019 CERES EBAF cloud property data, we examined the CRE global distribution. SH expansion of cloud properties with maximum degree 100 in total 5151 coefficients, can model CRE with errors less than 4.3 W m^{-2} in SW and 1.7 W m^{-2} in LW in more than 95% regions.

The SH power spectrum of a variable quantifies the contributions of individual SH components to the global distribution of the variable, and can be computed using SH expansion coefficients. We find that the SH power spectra of annual mean CRE have similar shapes in all years from 2001 to 2020. However, the power spectra for different variables at the same expansion degree have some variations. The SW CRE SH power spectrum shape is similar to that of the low and midlevel cloud water path (CWP), and the LW CRE SH power spectrum

shape is similar to that of the high CWP. This difference of SW and LW SH power spectra is consistent with the previous studies on the impact of cloud height on SW and LW CRE.

The variation of the CRE SH power spectrum is correlated with large-scale atmospheric circulation such as ENSO and HC. In particular, the anomalies of the CRE $l = 2$ power spectrum component are strongly correlated with the Multivariate ENSO Index (Wolter and Timlin, 1998, 2011). The $l = 2$ SH component of SW (LW) CRE anomalies are positive (negative) over Indonesia, the western Pacific and South America, and negative (positive) over the central and eastern Pacific and Africa. The anomaly patterns can be explained by the mechanism of ENSO's impact on clouds suggested by previous studies. The CRE $l = 3$ and $l = 5$ SH power spectrum components are found to be strongly correlated with the HC intensity, whereas the $l = 6$ and $l = 8$ components are correlated with variations in the HC latitudinal widths. The impact of ENSO on the HC can be observed in opposite anomaly patterns of those SH components in ENSO warm versus cold phases.

In summary, the SH expansion technique can be a useful tool to study a variable such as CRE that has global valid values, by decomposing it into different SH components. As we illustrated in this study, the effects of large-scale atmospheric circulation phenomena such as ENSO and HC can be interpreted from the SH power spectrum and individual SH components of CRE. The SH expansion technique provides an alternative perspective to study the variability of global geophysical parameters such as cloud properties and cloud radiative effects.

Acknowledgments

This work is supported by Texas A&M T3 grant 02-243685-00000. The computations were conducted at the Texas A&M University High Performance Research Computing facilities. Some of the results in this paper have been derived using the healpy and HEALPix package. The authors thank Steven R. Schroeder for helping check the grammar. Jiachen Ding thanks Jian Wei and Tong Ren for helpful discussions on RRTMG usage, ENSO and Hadley Circulation. Loeb, Smith, and Minnis are supported by the CERES Project.

Open Research

The CERES EBAF datasets used to obtain cloud property data are publicly available via the CERES project website https://ceres.larc.nasa.gov/data/. The ERA5 datasets used to obtain atmospheric profile and surface albedo are publicly available via the Climate Data Store from DOI: 10.24381/cds.6860a573 and DOI: 10.24381/cds.f17050d7. The CAMS datasets used to obtain CO_2, CH_4, and CO concentrations are publicly available via the Atmosphere Data Store (https://ads.atmosphere.copernicus.eu/). The MEI time series is publicly available via the website https://psl.noaa.gov/enso/mei/.

The HEALPix software used to compute spherical harmonic expansion is publicly available via https://healpix.sourceforge.net/ and https://github.com/healpy/healpy/. The

RRTMG software used to compute radiative flux is publicly available via https://github.com/AER-RC/RRTMG_LW and https://github.com/AER-RC/RRTMG_SW.

References

Abramo, L. R., & Pereira, T. S. (2010). Testing gaussianity, homogeneity, and isotropy with the cosmic microwave background. *Advances in Astronomy*, *2010*(1), 1–25. https://doi.org/10.1155/2010/378203

Allan, R. P., Slingo, A., & Ringer, M. A. (2002). Influence of dynamics on the changes in tropical cloud radiative forcing during the 1998 El Niño. *Journal of Climate*, *15*(14), 1979–1986. https://doi.org/10.1175/1520-0442(2002)015<1979:IODOTC>2.0.CO;2

Burleyson, C. D., Long, C. N., & Comstock, J. M. (2015). Quantifying diurnal cloud radiative effects by cloud type in the tropical western Pacific. *Journal of Applied Meteorology and Climatology*, *54*(6), 1297–1312. https://doi.org/10.1175/JAMC-D-14-0288.1

Cess, R. D., Zhang, M., Wang, P.-H., & Wielicki, B. A. (2001a). Cloud structure anomalies over the tropical Pacific during the 1997/98 El Niño. *Geophysical Research Letters*, *28*(24), 4547–4550. https://doi.org/10.1029/2001GL013750

Cess, R. D., Zhang, M., Wielicki, B. A., Young, D. F., Zhou, X.-L., & Nikitenko, Y. (2001b). The influence of the 1998 El Niño upon cloud-radiative forcing over the Pacific Warm Pool. *Journal of Climate*, *14*(9), 2129–2137. https://doi.org/10.1175/1520-0442(2001)014<2129:TIOTEN>2.0.CO;2

Cheng, M., Ries, J. C., & Tapley, B. D. (2011). Variations of the Earth's figure axis from satellite laser ranging and GRACE. *Journal of Geophysical Research*, *116*(B1), B01409. https://doi.org/10.1029/2010JB000850

Cheng, M., Tapley, B. D., & Ries, J. C. (2013). Deceleration in the Earth's oblateness. *Journal of Geophysical Research: Solid Earth*, *118*(2), 740–747. https://doi.org/10.1002/jgrb.50058

Clough, S. A., Shephard, M. W., Mlawer, E. J., Delamere, J. S., Iacono, M. J., Cady-Pereira, K., et al. (2005). Atmospheric radiative transfer modeling: A summary of the AER codes. *Journal of Quantitative Spectroscopy and Radiative Transfer*, *91*(2), 233–244. https://doi.org/10.1016/j.jqsrt.2004.05.058

Eastman, R., Warren, S. G., & Hahn, C. J. (2011). Variations in cloud cover and cloud types over the ocean from surface observations, 1954–2008. *Journal of Climate*, *24*(22), 5914–5934. https://doi.org/10.1175/2011JCLI3972.1

ECMWF. (2020). IFS documentation – Cy47r1: Part IV : Physical processes. (pp. 29–30). ECMWF. https://doi.org/10.21957/cpmkqvhja

Eliasen, E., Machenhauer, B., & Rasmussen, E. (1970). *On a Numerical Method for Integration of the Hydrodynamical Equations with a Spectral Representation of the Horizontal Fields* (Report 2, pp. 37). Institut for Teoretisk Meteorologi, University of Copenhagen. https://doi.org/10.13140/RG.2.2.13894.88645

Fu, Q., Liou, K. N., Cribb, M. C., Charlock, T. P., & Grossman, A. (1997). Multiple scattering parameterization in thermal infrared radiative transfer. *Journal of the Atmospheric Sciences*, *54*(24), 2799-2812. https://doi.org/10.1175/1520-0469(1997)054<2799:MSPITI>2.0.CO;2

Gorski, K. M., Hivon, E., Banday, A. J., Wandelt, B. D., Hansen, F. K., Reinecke, M., & Bartelmann, M. (2005). HEALPix: A framework for high-resolution discretization and fast analysis of data distributed on the sphere. *The Astrophysical Journal*, *622*(2), 759–771. https://doi.org/10.1086/427976

Gu, B., Ren, T., Kuo, C. P., Yang, P., & Bowman, K. (2021). Global impact of cloud longwave scattering in an atmosphere-only general circulation model simulation. *Journal of Geophysical Research: Atmospheres*, *126*(3), 1–20. https://doi.org/10.1029/2020JD033968

Gupta, S. K., Kratz, D., Stackhouse, P. W., & Wilber, A. C. (2001). *The Langley Parameterized Shortwave Algorithm (LPSA) for surface radiation budget studies (Version 1.0)*. Hampton, VA: NASA Langley Research Center.

Harrop, B. E., & Hartmann, D. L. (2016). The role of cloud radiative heating within the atmosphere on the high cloud amount and top-of-atmosphere cloud radiative effect. *Journal of Advances in Modeling Earth Systems*, *8*(3), 1391–1410. https://doi.org/10.1002/2016MS000670

Hartmann, D. L., Ockert-Bell, M. E., & Michelsen, M. L. (1992). The effect of cloud type on Earth's energy balance: Global analysis. *Journal of Climate*, *5*(11), 1281–1304. https://doi.org/10.1175/1520-0442(1992)005<1281:TEOCTO>2.0.CO;2

Hersbach, H., Bell, B., Berrisford, P., Hirahara, S., Horányi, A., Muñoz-Sabater, J., et al. (2020). The ERA5 global reanalysis. *Quarterly Journal of the Royal Meteorological Society*, *146*(730), 1999–2049. https://doi.org/10.1002/qj.3803

Hu, W., Fukugita, M., Zaldarriaga, M., & Tegmark, M. (2001). Cosmic microwave background observables and their cosmological implications. *The Astrophysical Journal*, *549*(2), 669–680. https://doi.org/10.1086/319449

Iacono, M. J., Delamere, J. S., Mlawer, E. J., Shephard, M. W., Clough, S. A., & Collins, W. D. (2008). Radiative forcing by long-lived greenhouse gases: Calculations with the AER radiative transfer models. *Journal of Geophysical Research*, *113*(D13), D13103. https://doi.org/10.1029/2008JD009944

Inness, A., Ades, M., Agustí-Panareda, A., Barré, J., Benedictow, A., Blechschmidt, A.-M., et al. (2019). The CAMS reanalysis of atmospheric composition. *Atmospheric Chemistry and Physics*, *19*(6), 3515–3556. https://doi.org/10.5194/acp-19-3515-2019

Kamionkowski, M., Kosowsky, A., & Stebbins, A. (1997). Statistics of cosmic microwave background polarization. *Physical Review D*, *55*(12), 7368–7388. https://doi.org/10.1103/PhysRevD.55.7368

Kato, S., Rose, F. G., Rutan, D. A., Thorsen, T. J., Loeb, N. G., Doelling, D. R., et al. (2018). Surface irradiances of Edition 4.0 Clouds and the Earth's Radiant Energy System (CERES) Energy Balanced and Filled (EBAF) data product. *Journal of Climate*, *31*(11), 4501–4527. https://doi.org/10.1175/JCLI-D-17-0523.1

583 Kaula, W. M. (1959). Statistical and harmonic analysis of gravity. *Journal of Geophysical*
584 *Research*, *64*(12), 2401–2421. https://doi.org/10.1029/JZ064i012p02401

585 Klein, S. A., Soden, B. J., & Lau, N.-C. (1999). Remote sea surface temperature variations
586 during ENSO: Evidence for a tropical atmospheric bridge. *Journal of Climate*, *12*(4),
587 917–932. https://doi.org/10.1175/1520-0442(1999)012<0917:RSSTVD>2.0.CO;2

588 Koppelt, U., Biegel, M., & Pěč, K. (1989). Spherical harmonic expansion of the continents and
589 oceans distribution function. *Studia Geophysica et Geodaetica*, *33*(4), 315–321.
590 https://doi.org/10.1007/BF01637687

591 Kuo, C. P., Yang, P., Huang, X., Chen, Y. H., & Liu, G. (2020). Assessing the accuracy and
592 efficiency of longwave radiative transfer models involving scattering effect with cloud
593 optical property parameterizations. *Journal of Quantitative Spectroscopy and Radiative*
594 *Transfer*, *240*, 106683. https://doi.org/10.1016/j.jqsrt.2019.106683

595 Kuo, C. P., Yang, P., Huang, X., Feldman, D., Flanner, M., Kuo, C., & Mlawer, E. J. (2017).
596 Impact of multiple scattering on longwave radiative transfer involving clouds. *Journal of*
597 *Advances in Modeling Earth Systems*, *9*(8), 3082–3098.
598 https://doi.org/10.1002/2017MS001117

599 Loeb, N. G., Doelling, D. R., Wang, H., Su, W., Nguyen, C., Corbett, J. G., et al. (2018a).
600 Clouds and the Earth's Radiant Energy System (CERES) Energy Balanced and Filled
601 (EBAF) Top-of-Atmosphere (TOA) Edition-4.0 data product. *Journal of Climate*, *31*(2),
602 895–918. https://doi.org/10.1175/JCLI-D-17-0208.1

603 Loeb, N. G., Rutan, D. A., Kato, S., & Wang, W. (2014). Observing interannual variations in
604 Hadley circulation atmospheric diabatic heating and circulation strength. *Journal of*
605 *Climate*, *27*(11), 4139–4158. https://doi.org/10.1175/JCLI-D-13-00656.1

606 Loeb, N. G., Yang, P., Rose, F. G., Hong, G., Sun-Mack, S., Minnis, P., et al. (2018b). Impact of
607 ice cloud microphysics on satellite cloud retrievals and broadband flux radiative transfer
608 model calculations. *Journal of Climate*, *31*(5), 1851–1864. https://doi.org/10.1175/JCLI-
609 D-17-0426.1

610 Marchand, R. (2013). Trends in ISCCP, MISR, and MODIS cloud-top-height and optical-depth
611 histograms. *Journal of Geophysical Research: Atmospheres*, *118*(4), 1941–1949.
612 https://doi.org/10.1002/jgrd.50207

613 Moore, R. W., & Vonder Haar, T. H. (2001). Interannual variability of cloud forcing and
614 meridional energy transport for the Northern Hemisphere winter from 1984 to 1990.
615 *Journal of Climate*, *14*(17), 3643–3654. https://doi.org/10.1175/1520-
616 0442(2001)014<3643:IVOCFA>2.0.CO;2

617 Nerem, R. S., Jekeli, C., & Kaula, W. M. (1995). Gravity field determination and characteristics:
618 Retrospective and prospective. *Journal of Geophysical Research: Solid Earth*, *100*(B8),
619 15053–15074. https://doi.org/10.1029/94JB03257

620 Nguyen, H., Evans, A., Lucas, C., Smith, I., & Timbal, B. (2013). The Hadley circulation in
621 reanalyses: Climatology, variability, and change. *Journal of Climate*, *26*(10), 3357–3376.
622 https://doi.org/10.1175/JCLI-D-12-00224.1

623 Norris, J. R. (2005). Trends in upper-level cloud cover and surface divergence over the tropical
624 Indo-Pacific Ocean between 1952 and 1997. *Journal of Geophysical Research*,
625 *110*(D21), D21110. https://doi.org/10.1029/2005JD006183

626 Oort, A. H., & Yienger, J. J. (1996). Observed interannual variability in the Hadley Circulation
627 and its connection to ENSO. *Journal of Climate*, *9*(11), 2751–2767.
628 https://doi.org/10.1175/1520-0442(1996)009<2751:OIVITH>2.0.CO;2

629 Orszag, S. A. (1970). Transform method for the calculation of vector-coupled sums: Application
630 to the spectral form of the vorticity equation. *Journal of the Atmospheric Sciences*, *27*(6),
631 890–895. https://doi.org/10.1175/1520-0469(1970)027<0890:TMFTCO>2.0.CO;2

632 Park, S., & Leovy, C. B. (2004). Marine low-cloud anomalies associated with ENSO. *Journal of*
633 *Climate*, *17*(17), 3448–3469. https://doi.org/10.1175/1520-
634 0442(2004)017<3448:MLAAWE>2.0.CO;2

635 Pincus, R., Barker, H. W., & Morcrette, J.-J. (2003). A fast, flexible, approximate technique for
636 computing radiative transfer in inhomogeneous cloud fields. *Journal of Geophysical*
637 *Research: Atmospheres*, *108*(D13), 1–5. https://doi.org/10.1029/2002JD003322

638 Platnick, S., Meyer, K. G., King, M. D., Wind, G., Amarasinghe, N., Marchant, B., et al. (2017).
639 The MODIS cloud optical and microphysical products: Collection 6 updates and
640 examples from Terra and Aqua. *IEEE Transactions on Geoscience and Remote Sensing*,
641 *55*(1), 502–525. https://doi.org/10.1109/TGRS.2016.2610522

642 Platzman, G. W. (1960). The spectral form of the vorticity equation. *Journal of Meteorology*,
643 *17*(6), 635–644. https://doi.org/10.1175/1520-0469(1960)017<0635:TSFOTV>2.0.CO;2

644 Ramanathan, V., Cess, R. D., Harrison, E. F., Minnis, P., Barkstrom, B. R., Ahmad, E., &
645 Hartmann, D. (1989). Cloud-radiative forcing and climate: Results from the Earth
646 Radiation Budget Experiment. *Science*, *243*(4887), 57–63.
647 https://doi.org/10.1126/science.243.4887.57

648 Stachnik, J. P., & Schumacher, C. (2011). A comparison of the Hadley circulation in modern
649 reanalyses. *Journal of Geophysical Research: Atmospheres*, *116*(D22), D22102.
650 https://doi.org/10.1029/2011JD016677

651 Stephens, G. L., Li, J., Wild, M., Clayson, C. A., Loeb, N., Kato, S., et al. (2012). An update on
652 Earth's energy balance in light of the latest global observations. *Nature Geoscience*,
653 *5*(10), 691–696. https://doi.org/10.1038/ngeo1580

654 Stubenrauch, C. J., Rossow, W. B., Kinne, S., Ackerman, S., Cesana, G., Chepfer, H., et al.
655 (2013). Assessment of global cloud datasets from satellites: Project and database initiated
656 by the GEWEX radiation panel. *Bulletin of the American Meteorological Society*, *94*(7),
657 1031–1049. https://doi.org/10.1175/BAMS-D-12-00117.1

658 Suda, R., & Takami, M. (2001). A fast spherical harmonics transform algorithm. *Mathematics of*
659 *Computation*, *71*(238), 703–716. https://doi.org/10.1090/S0025-5718-01-01386-2

660 Tapley, B. D., Bettadpur, S., Watkins, M., & Reigber, C. (2004). The gravity recovery and
661 climate experiment: Mission overview and early results. *Geophysical Research Letters*,
662 *31*(9), L09607. https://doi.org/10.1029/2004GL019920

Tegmark, M., Zaldarriaga, M., & Hamilton, A. J. S. (2001). Towards a refined cosmic concordance model: Joint 11-parameter constraints from the cosmic microwave background and large-scale structure. *Physical Review D*, *63*(4), 043007. https://doi.org/10.1103/PhysRevD.63.043007

Toon, O. B., McKay, C. P., Ackerman, T. P., & Santhanam, K. (1989). Rapid calculation of radiative heating rates and photodissociation rates in inhomogeneous multiple scattering atmospheres. *Journal of Geophysical Research*, *94*(D13), 16287–16301. https://doi.org/10.1029/JD094iD13p16287

Trenberth, K. E., Fasullo, J. T., & Kiehl, J. (2009). Earth's global energy budget. *Bulletin of the American Meteorological Society*, *90*(3), 311–323. https://doi.org/10.1175/2008BAMS2634.1

Wang, X., Tegmark, M., & Zaldarriaga, M. (2002). Is cosmology consistent? *Physical Review D*, *65*(12), 123001. https://doi.org/10.1103/PhysRevD.65.123001

Wedi, N. P., Hamrud, M., & Mozdzynski, G. (2013). A fast spherical harmonics transform for global NWP and climate models. *Monthly Weather Review*, *141*(10), 3450–3461. https://doi.org/10.1175/MWR-D-13-00016.1

Williamson, D. L. (2007). The evolution of dynamical cores for global atmospheric models. *Journal of the Meteorological Society of Japan. Ser. II*, *85B*, 241–269. https://doi.org/10.2151/jmsj.85B.241

Wolter, K., & Timlin, M. S. (1998). Measuring the strength of ENSO events: How does 1997/98 rank? *Weather*, *53*(9), 315–324. https://doi.org/10.1002/j.1477-8696.1998.tb06408.x

Wolter, K., & Timlin, M. S. (2011). El Niño/Southern Oscillation behaviour since 1871 as diagnosed in an extended multivariate ENSO index (MEI.ext). *International Journal of Climatology*, *31*(7), 1074–1087. https://doi.org/10.1002/joc.2336

Yang, Y., Russell, L. M., Xu, L., Lou, S., Lamjiri, M. A., Somerville, R. C. J., et al. (2016). Impacts of ENSO events on cloud radiative effects in preindustrial conditions: Changes in cloud fraction and their dependence on interactive aerosol emissions and concentrations. *Journal of Geophysical Research: Atmospheres*, *121*(11), 6321–6335. https://doi.org/10.1002/2015JD024503

Yi, B., Rapp, A. D., Yang, P., Baum, B. A., & King, M. D. (2017). A comparison of Aqua MODIS ice and liquid water cloud physical and optical properties between collection 6 and collection 5.1: Pixel-to-pixel comparisons. *Journal of Geophysical Research: Atmospheres*, *122*(8), 4528–4549. https://doi.org/10.1002/2016JD025586

Zhang, T., Hoell, A., Perlwitz, J., Eischeid, J., Murray, D., Hoerling, M., & Hamill, T. M. (2019). Towards probabilistic multivariate ENSO monitoring. *Geophysical Research Letters*, *46*(17–18), 10532–10540. https://doi.org/10.1029/2019GL083946

Zhu, P., Hack, J. J., Kiehl, J. T., & Bretherton, C. S. (2007). Climate sensitivity of tropical and subtropical marine low cloud amount to ENSO and global warming due to doubled CO_2. *Journal of Geophysical Research*, *112*(D17), D17108. https://doi.org/10.1029/2006JD008174

Zonca, A., Singer, L., Lenz, D., Reinecke, M., Rosset, C., Hivon, E., & Gorski, K. (2019). Healpy: Equal area pixelization and spherical harmonics transforms for data on the sphere in Python. *Journal of Open Source Software*, *4*(35), 1298. https://doi.org/10.21105/joss.01298

Figure 1.

EBAF TOA CRE

(a)

−110 −70 −30 0 40 80

EBAF COD

(e)

0 5 10 15 20 25

$\Delta F_{CRE,L}$, $L = 100$

(b)

$\Delta \tau_L$, $L = 100$

(f)

$\Delta F_{CRE,L}$, $L = 200$

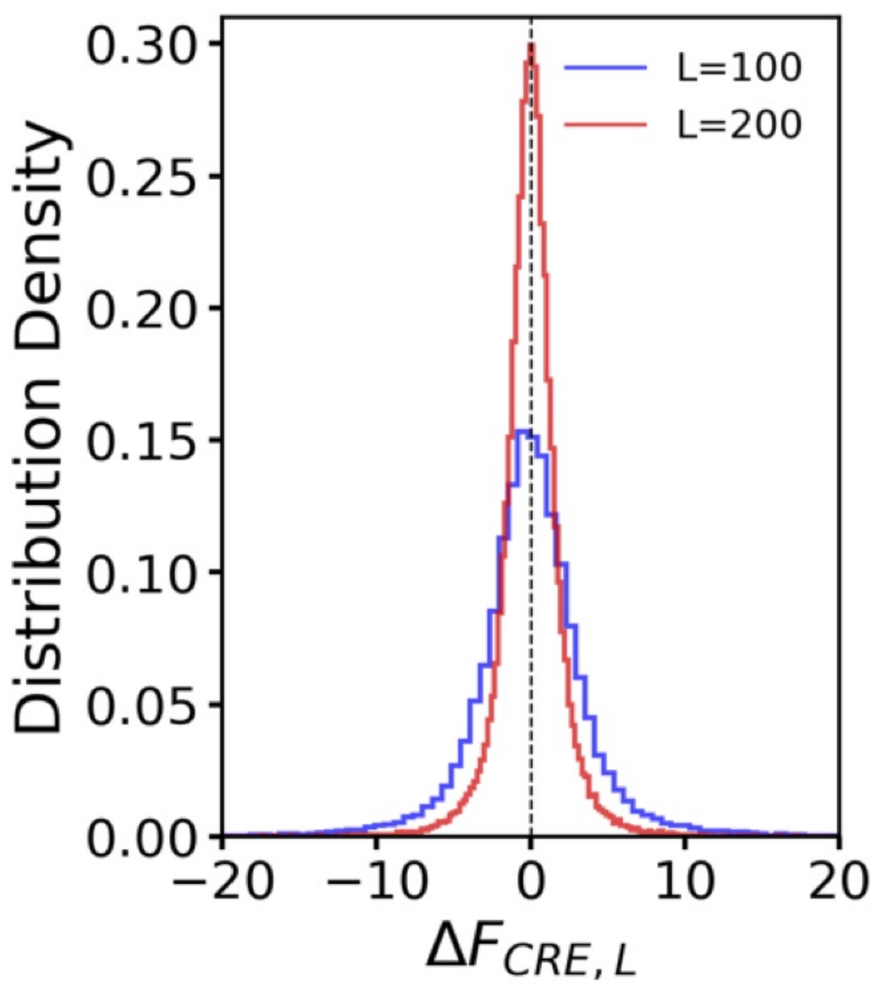
(c)

−20 −10 0 10 20

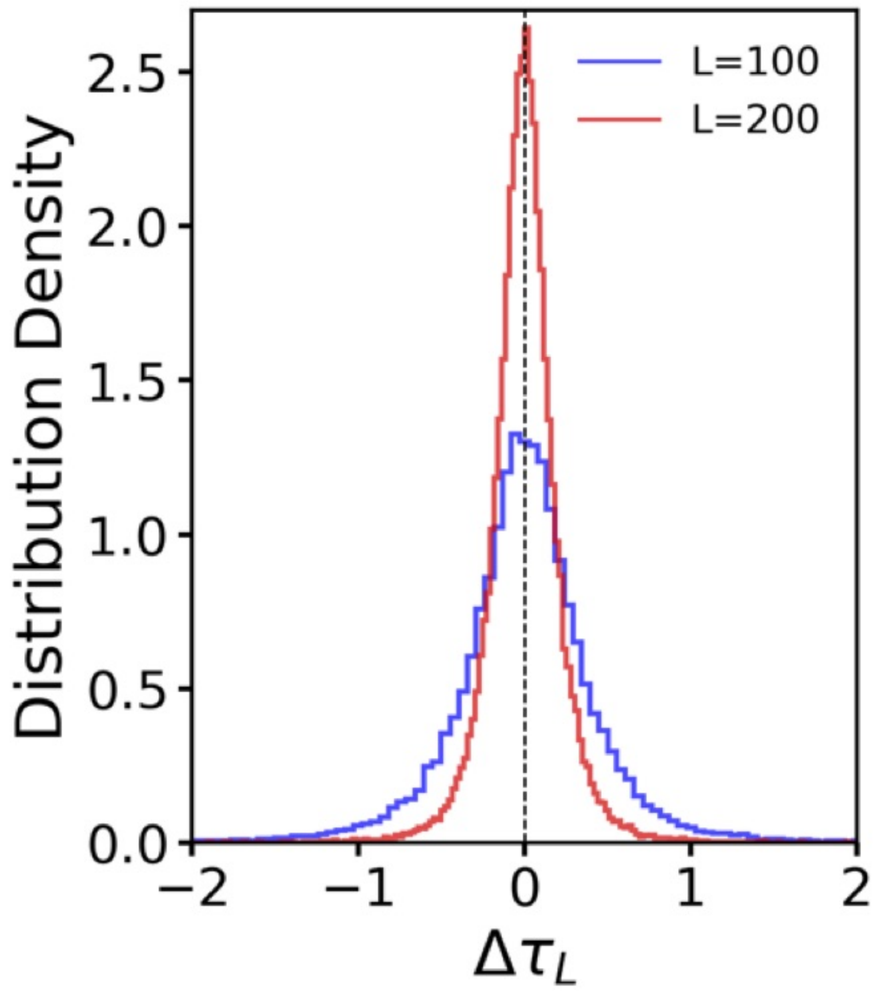
$\Delta \tau_L$, $L = 200$

(g)

−2 −1 0 1 2



(d)



(h)

Figure 2.

SW CRE, Original

LW CRE, Original

(a)

(b)

−150 −100 −50 0

−8 0 10 30 50 70

SW $\Delta F_{CRE,L}$, $L = 100$

LW $\Delta F_{CRE,L}$, $L = 100$

(c)

(d)

SW $\Delta F_{CRE,L}$, $L = 200$

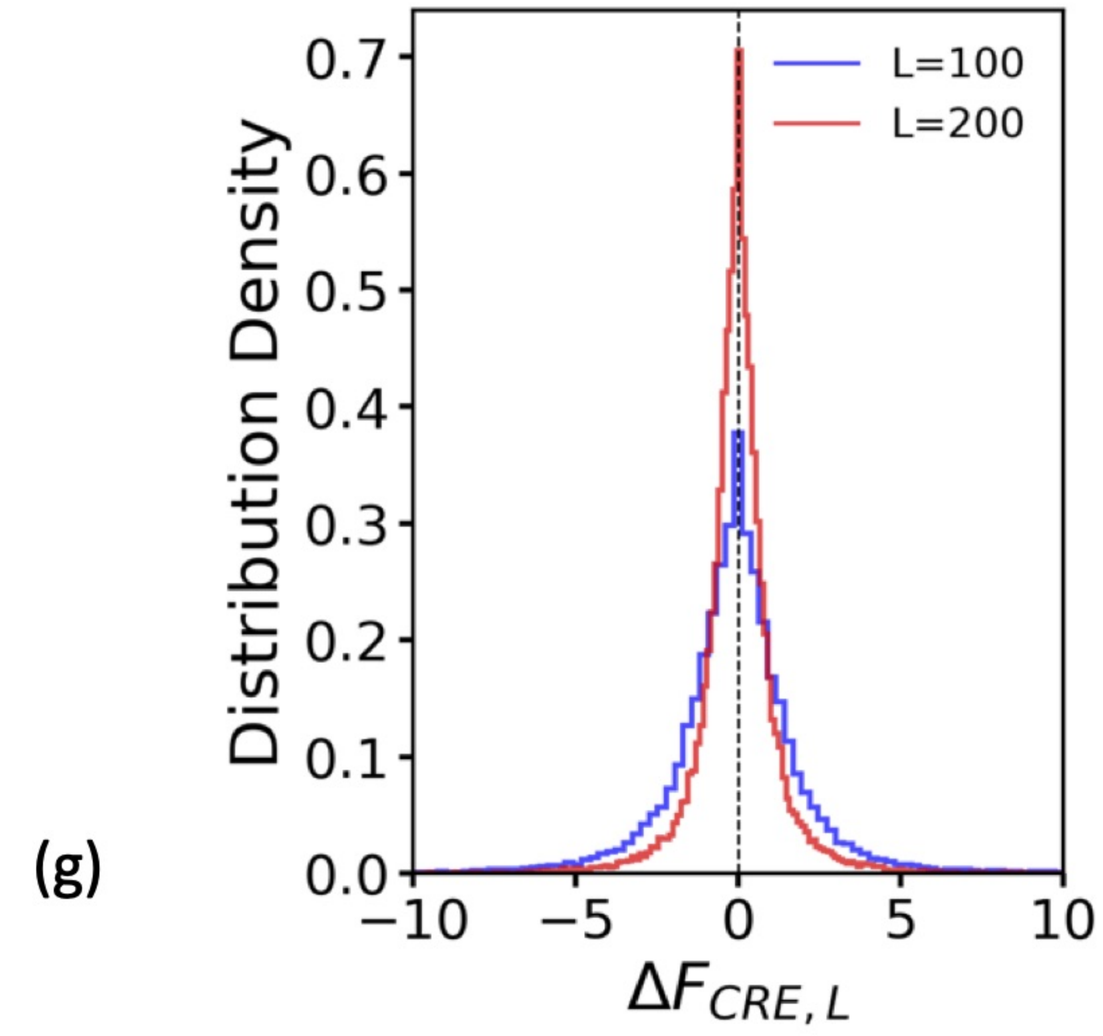
LW $\Delta F_{CRE,L}$, $L = 200$

(e)

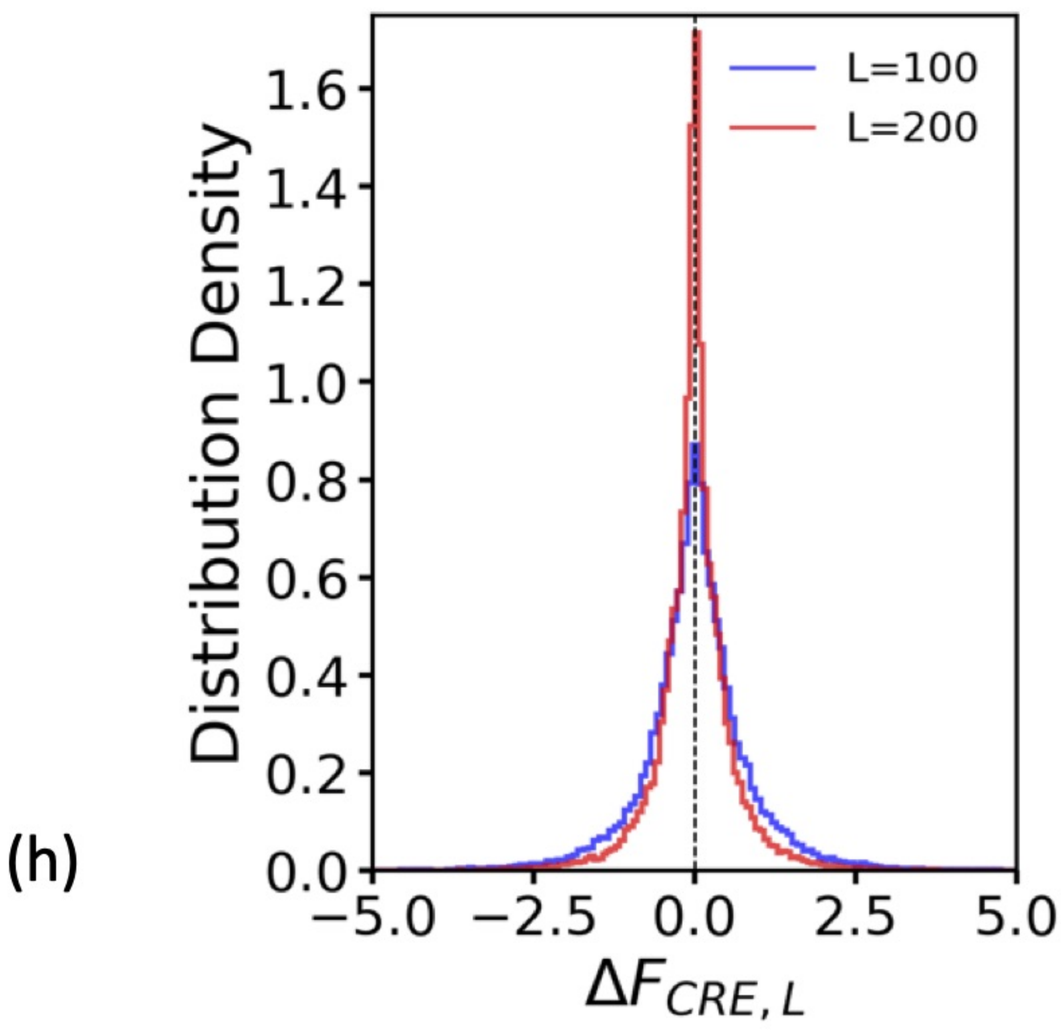
(f)

−25 −10 0 10 25

−9 −6 −3 0 3 6 9



(g)



(h)

Figure 3.

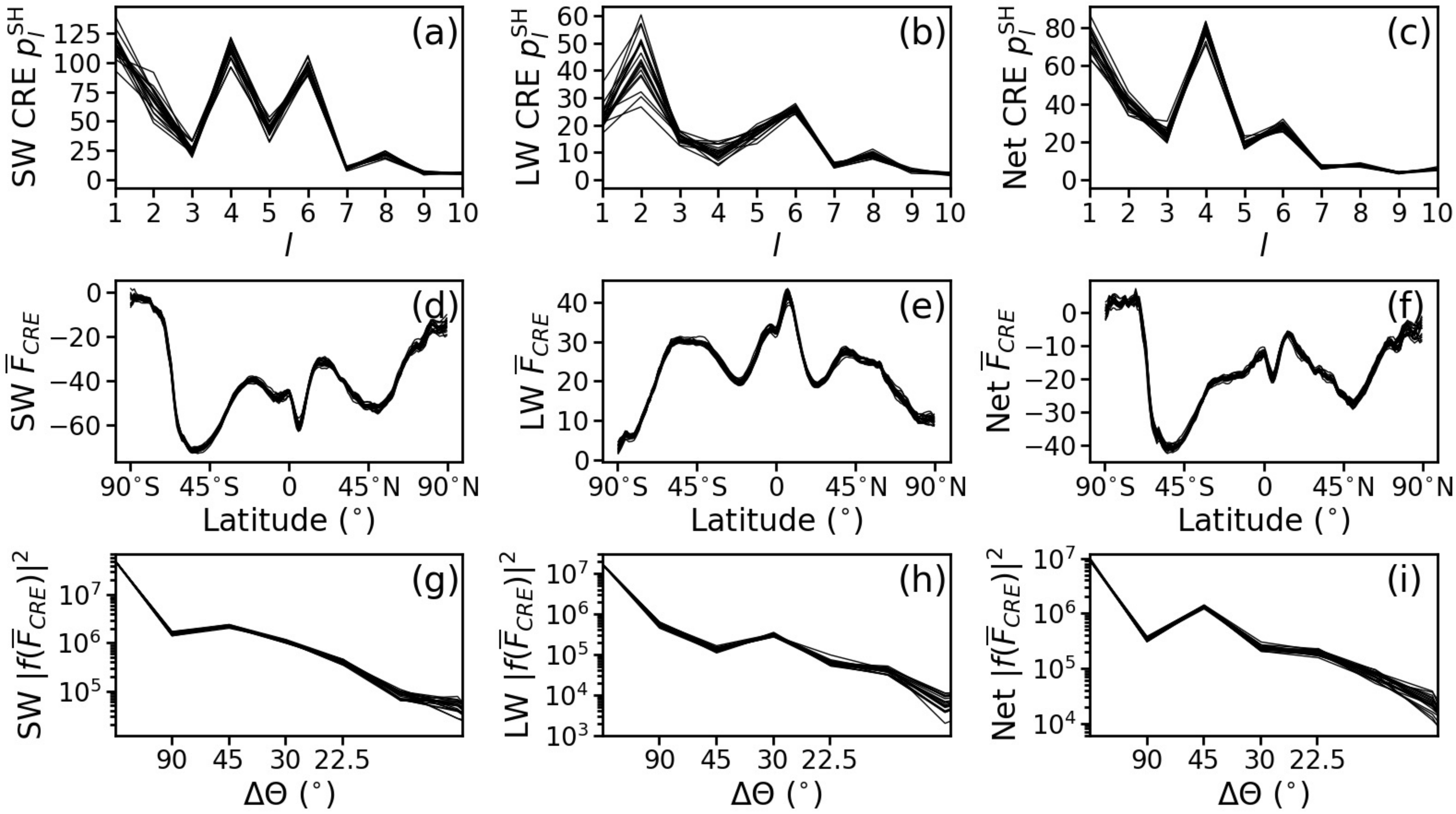

(a)
SW CRE p_l^{SH}
l
(b)
LW CRE p_l^{SH}
l
(c)
Net CRE p_l^{SH}
l
(d)
SW $\overline{F}_{CRE}$
90°S 45°S 0 45°N 90°N
Latitude (°)
(e)
LW $\overline{F}_{CRE}$
90°S 45°S 0 45°N 90°N
Latitude (°)
(f)
Net $\overline{F}_{CRE}$
90°S 45°S 0 45°N 90°N
Latitude (°)
(g)
SW $|f(\overline{F}_{CRE})|^2$
90 45 30 22.5
ΔΘ (°)
(h)
LW $|f(\overline{F}_{CRE})|^2$
90 45 30 22.5
ΔΘ (°)
(i)
Net $|f(\overline{F}_{CRE})|^2$
90 45 30 22.5
ΔΘ (°)

Figure 4.

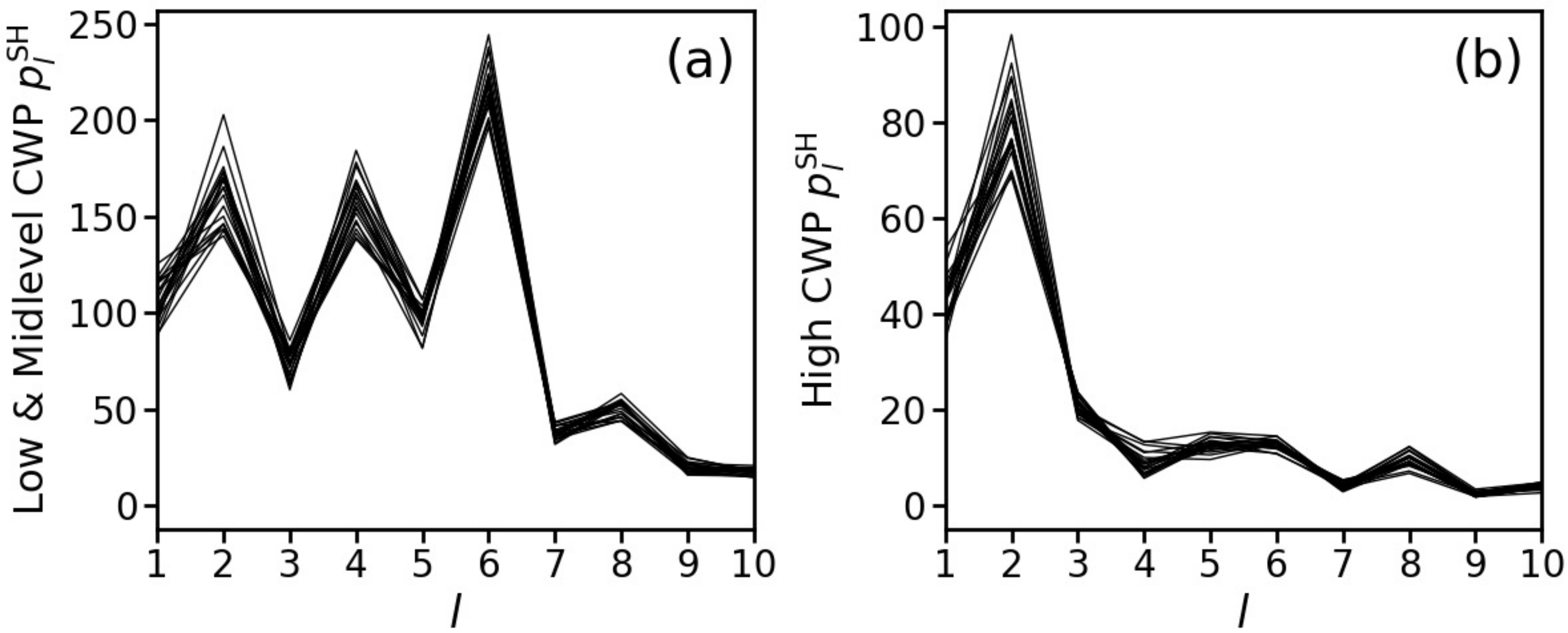

(a)
Low & Midlevel CWP p_l^{SH}
250
200
150
100
50
0
1
2
3
4
5
6
7
8
9
10
l
(b)
High CWP p_l^{SH}
100
80
60
40
20
0
1
2
3
4
5
6
7
8
9
10
l

Figure 5.

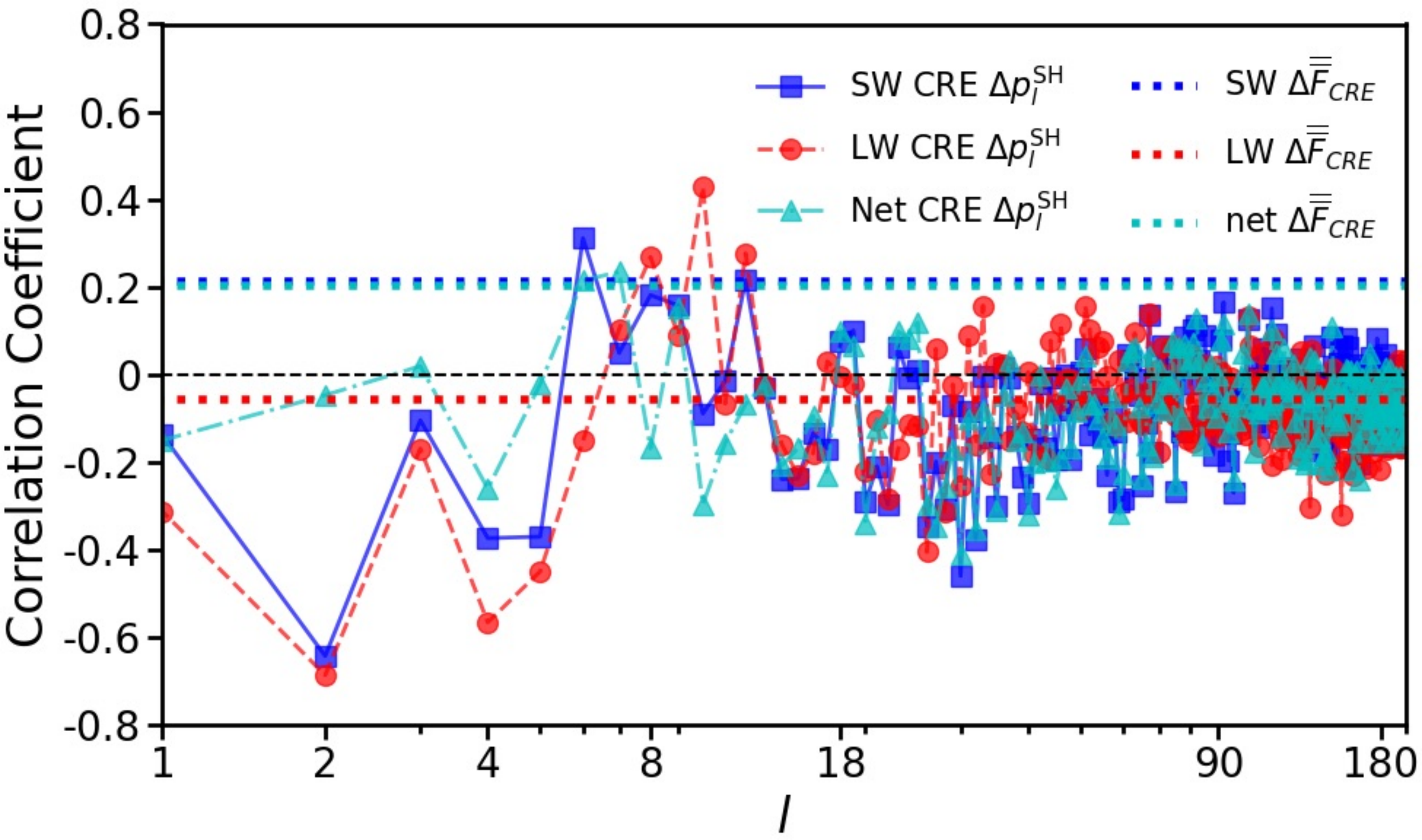

Correlation Coefficient
0.8
0.6
0.4
0.2
0
-0.2
-0.4
-0.6
-0.8
1
2
4
8
18
90
180
l
SW CRE Δp_l^{SH}
LW CRE Δp_l^{SH}
Net CRE Δp_l^{SH}
SW $\Delta\overline{\overline{F}}_{CRE}$
LW $\Delta\overline{\overline{F}}_{CRE}$
net $\Delta\overline{\overline{F}}_{CRE}$

Figure 6.

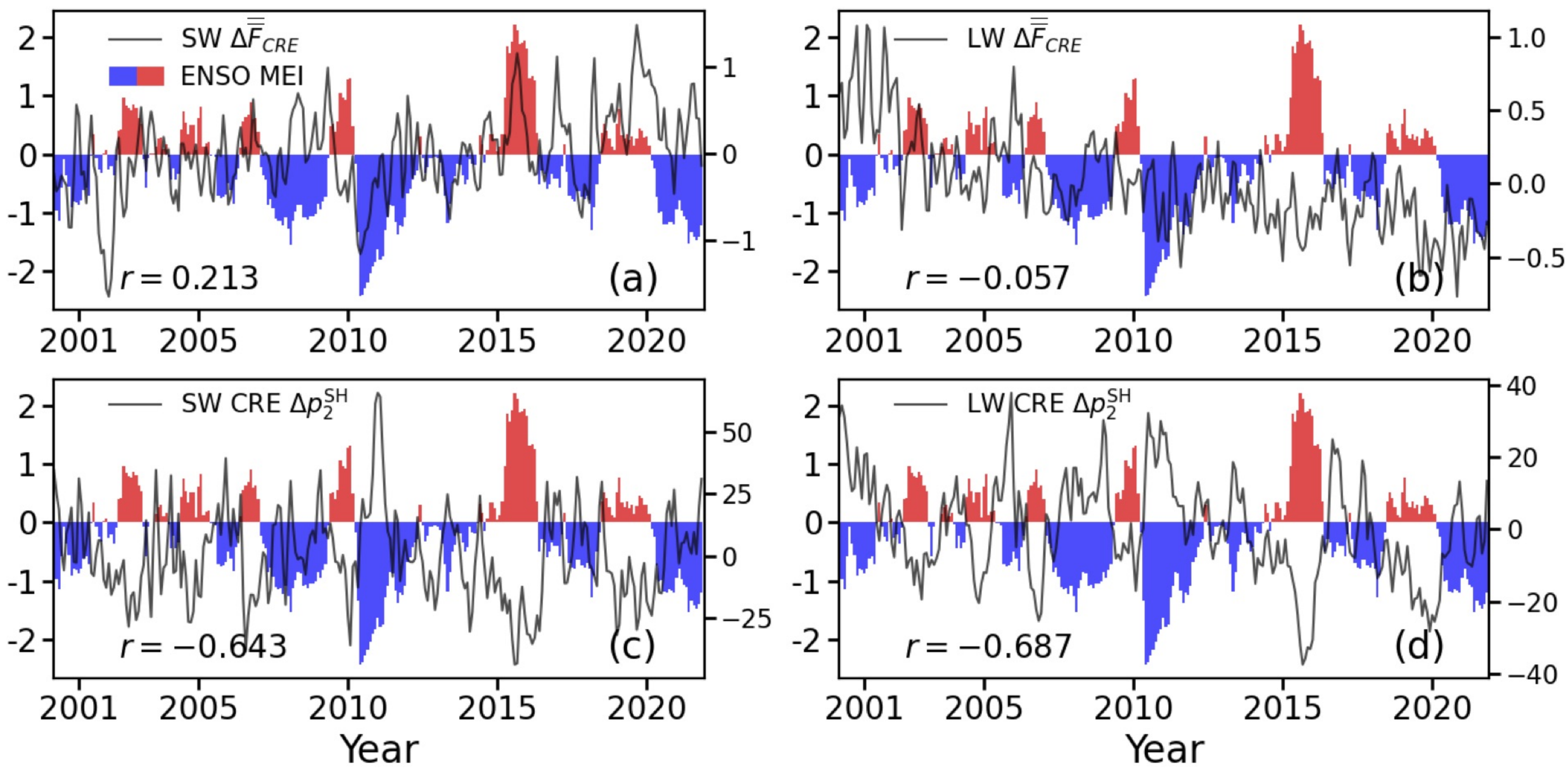
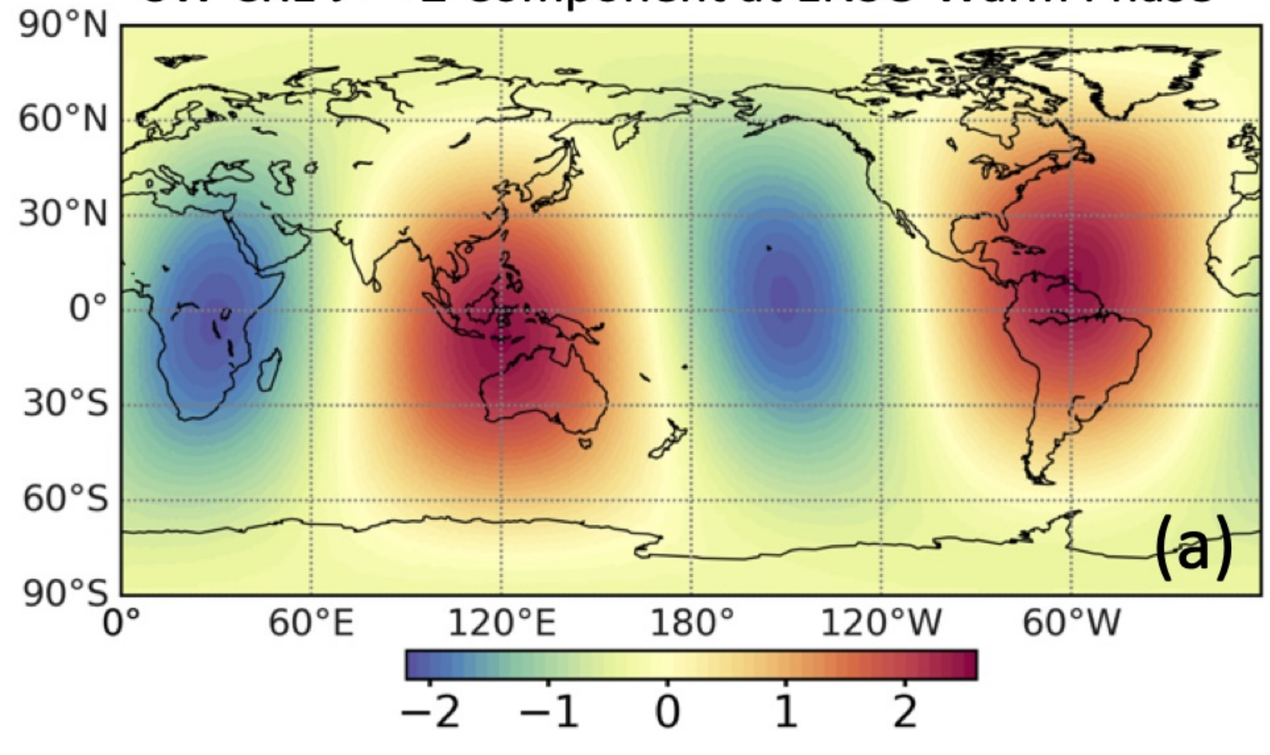
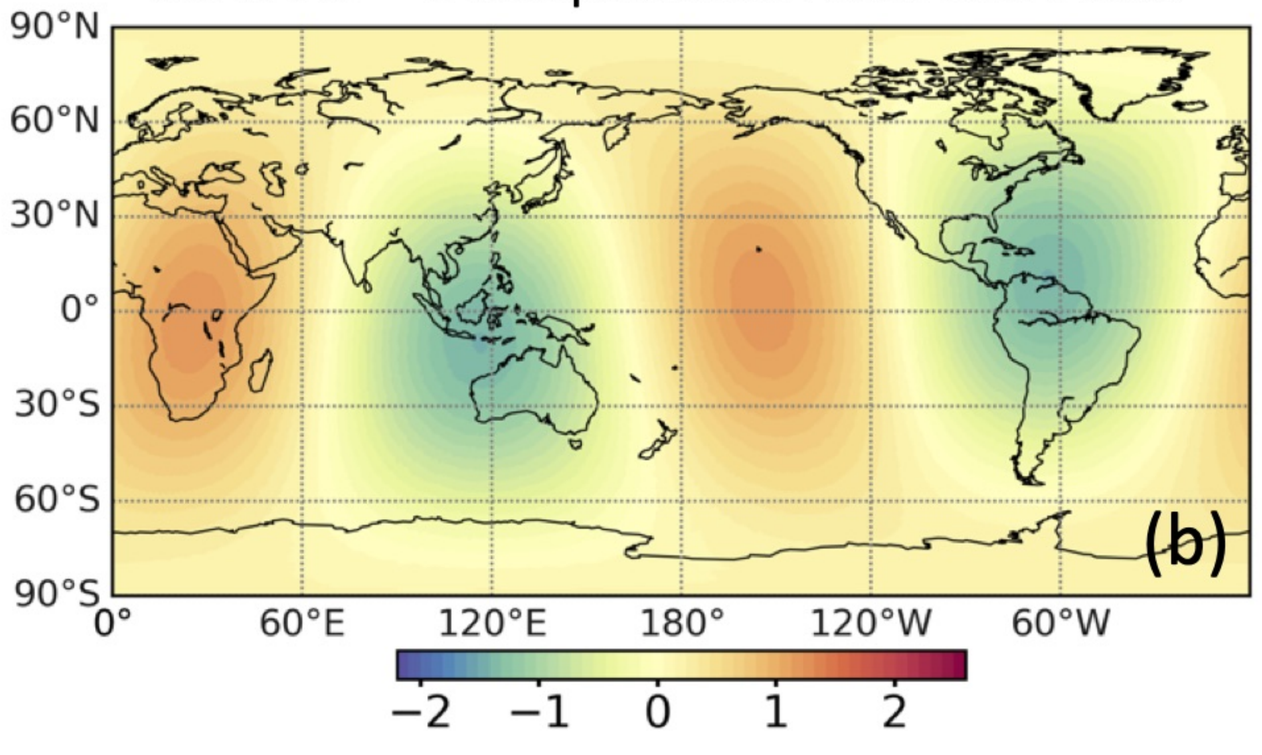

SW $\Delta\overline{\overline{F}}_{CRE}$
ENSO MEI
$r = 0.213$
(a)
LW $\Delta\overline{\overline{F}}_{CRE}$
$r = -0.057$
(b)
SW CRE Δp_2^{SH}
$r = -0.643$
(c)
LW CRE Δp_2^{SH}
$r = -0.687$
(d)
2001
2005
2010
2015
2020
Year

Figure 7.

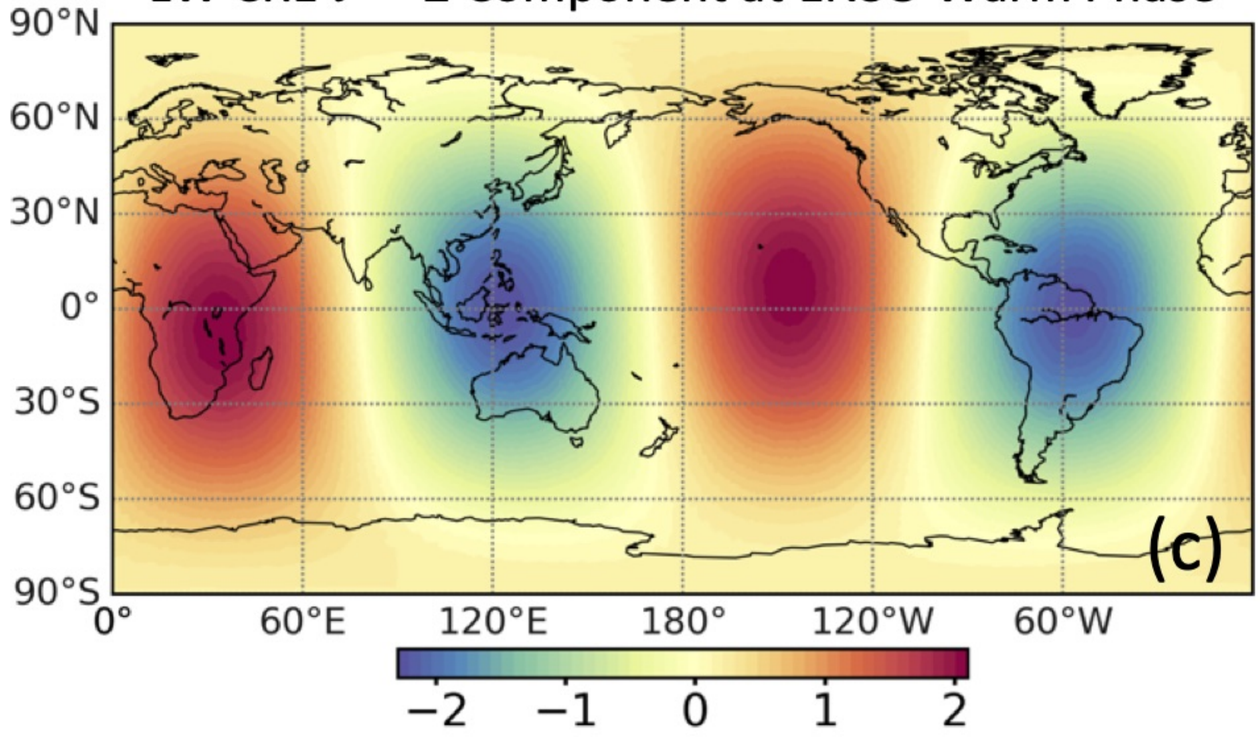
SW CRE $l = 2$ Component at ENSO Warm Phase



SW CRE $l = 2$ Component at ENSO Cold Phase



LW CRE $l = 2$ Component at ENSO Warm Phase



LW CRE $l = 2$ Component at ENSO Cold Phase

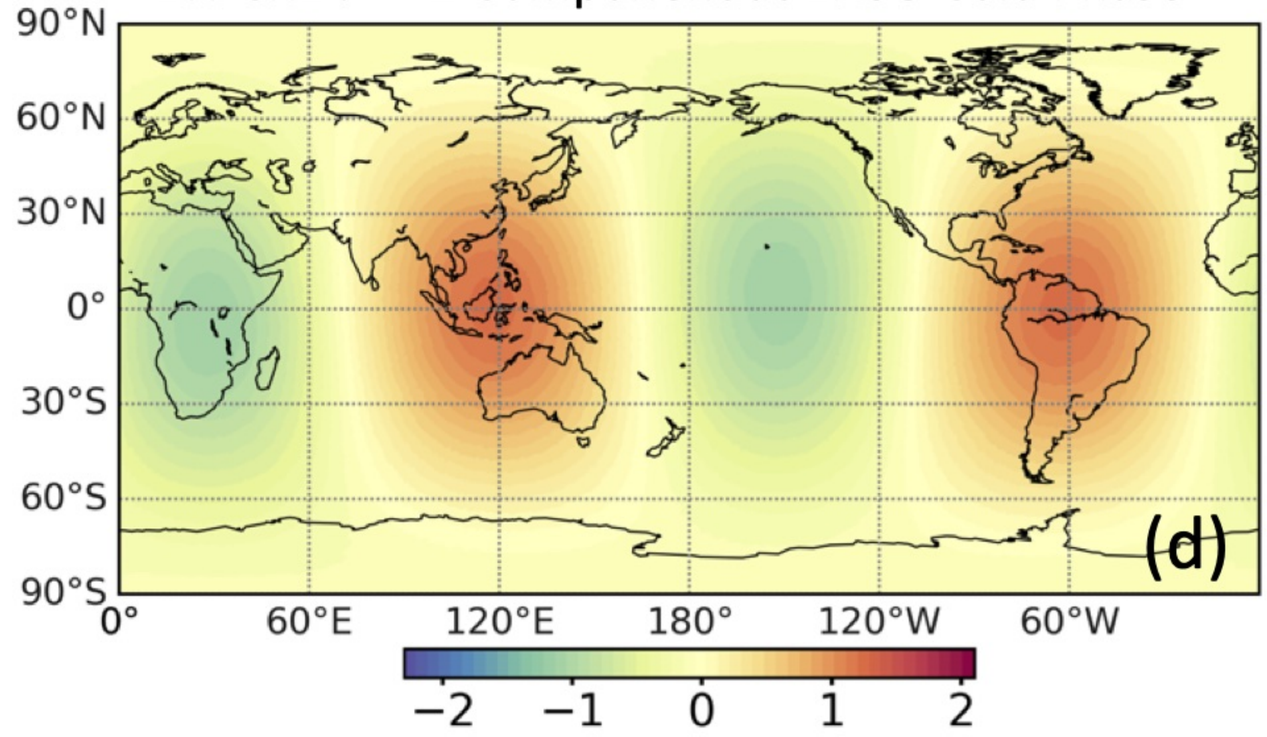


Figure 8.

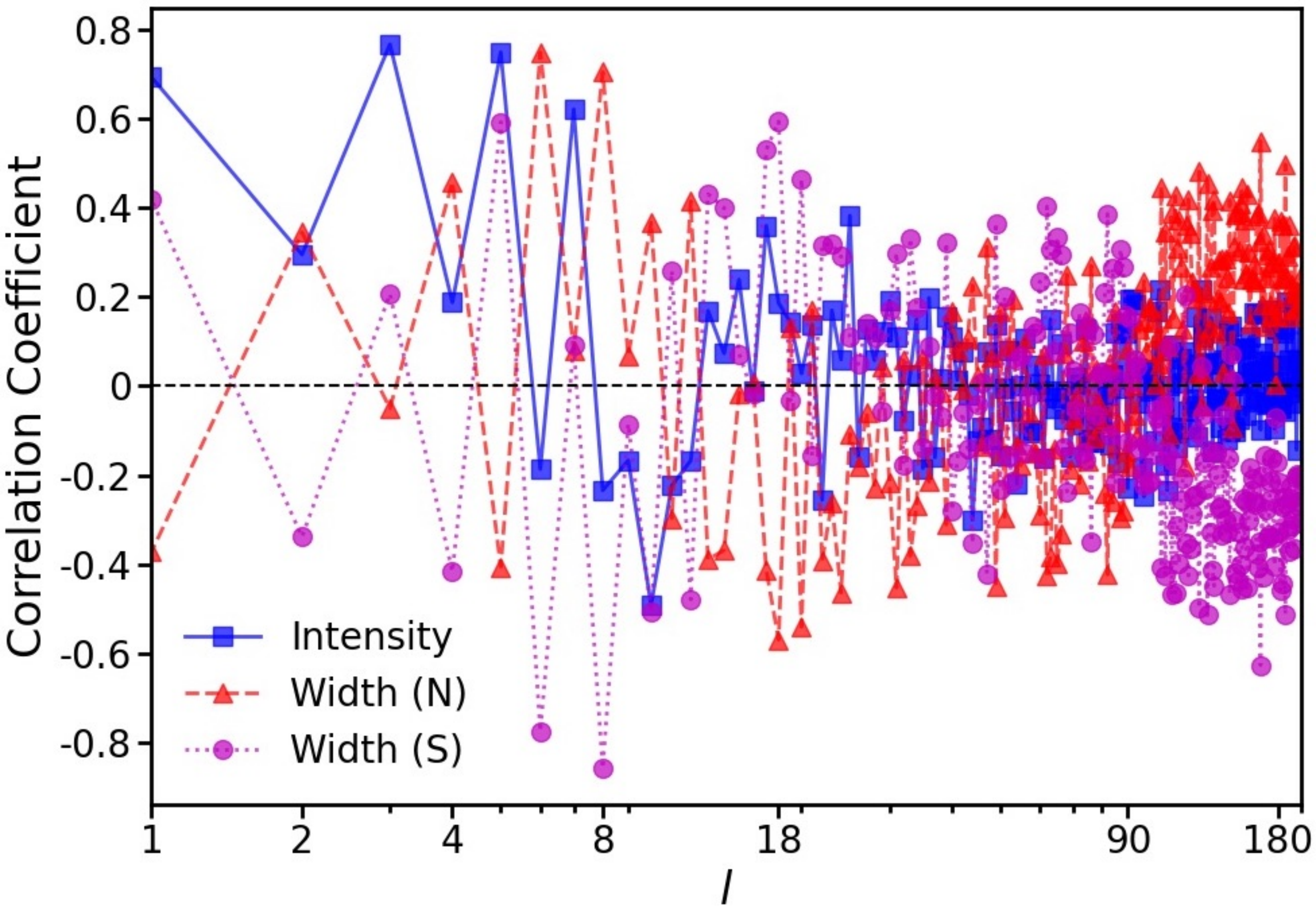

Correlation Coefficient
0.8
0.6
0.4
0.2
0
-0.2
-0.4
-0.6
-0.8
Intensity
Width (N)
Width (S)
1
2
4
8
18
90
180
l

Figure 9.

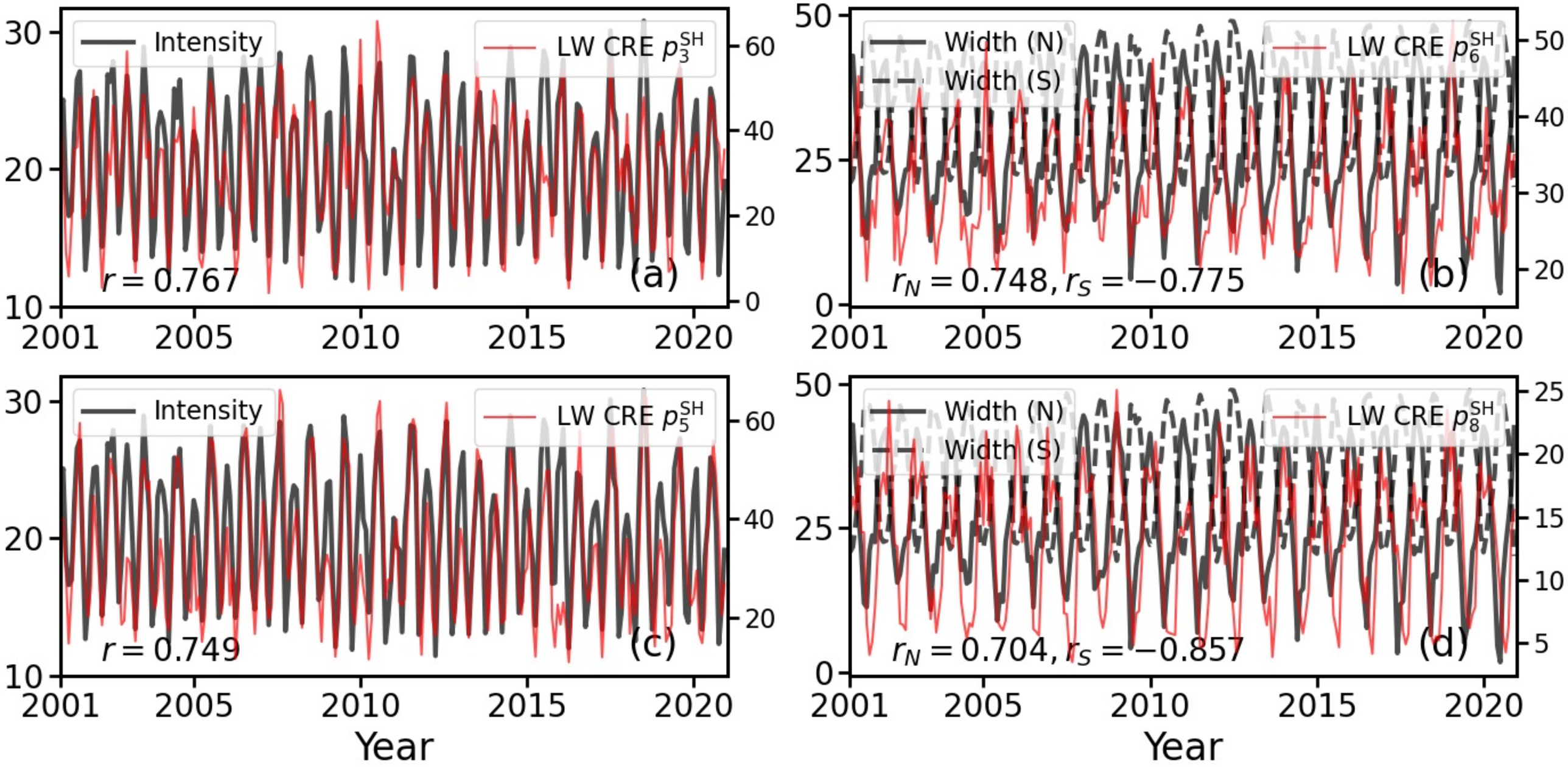
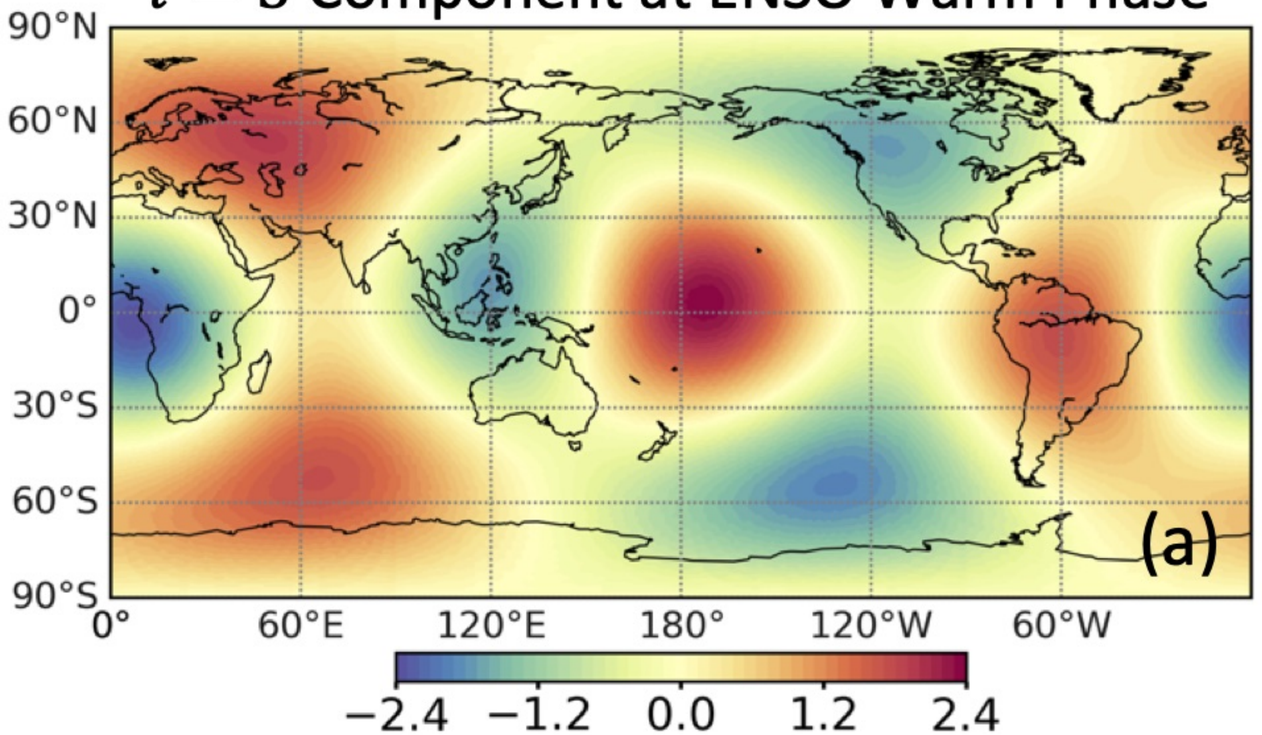
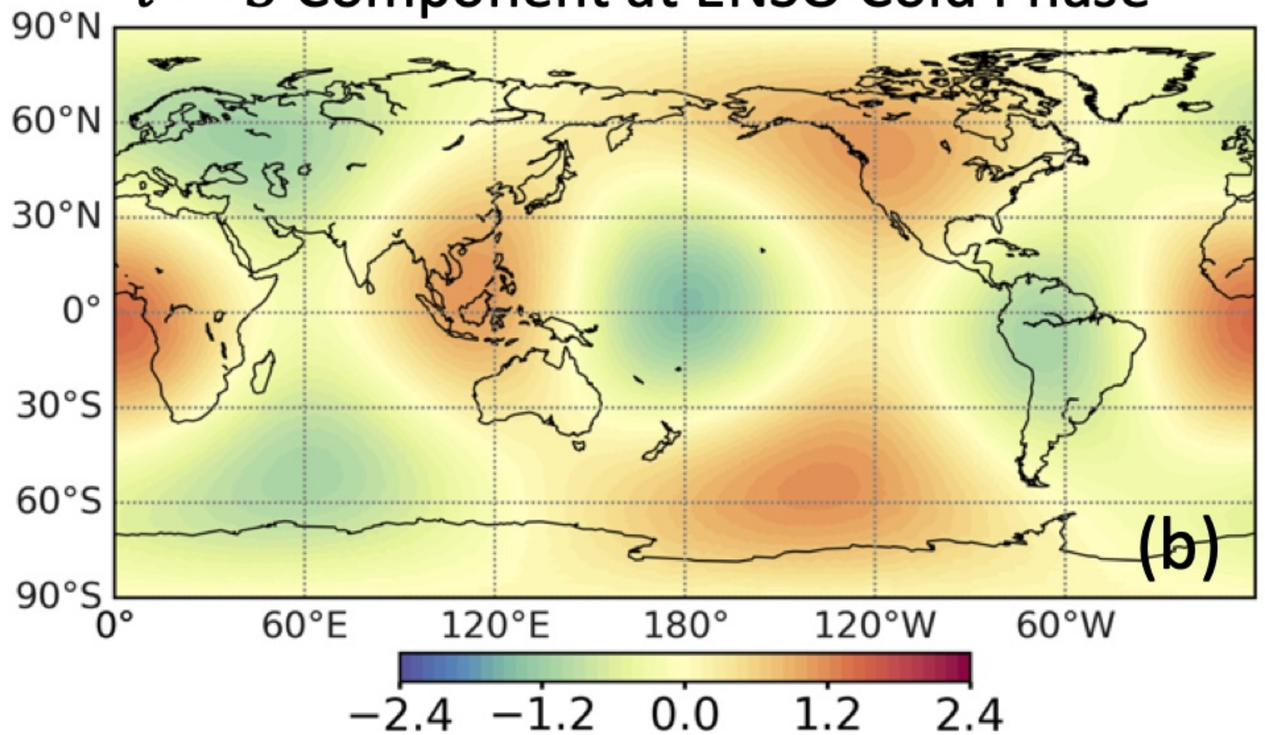

Intensity
LW CRE p_3^{SH}
$r = 0.767$
(a)
Width (N)
Width (S)
LW CRE p_6^{SH}
$r_N = 0.748, r_S = -0.775$
(b)
Intensity
LW CRE p_5^{SH}
$r = 0.749$
(c)
Width (N)
Width (S)
LW CRE p_8^{SH}
$r_N = 0.704, r_S = -0.857$
(d)
Year
Year

Figure 10.

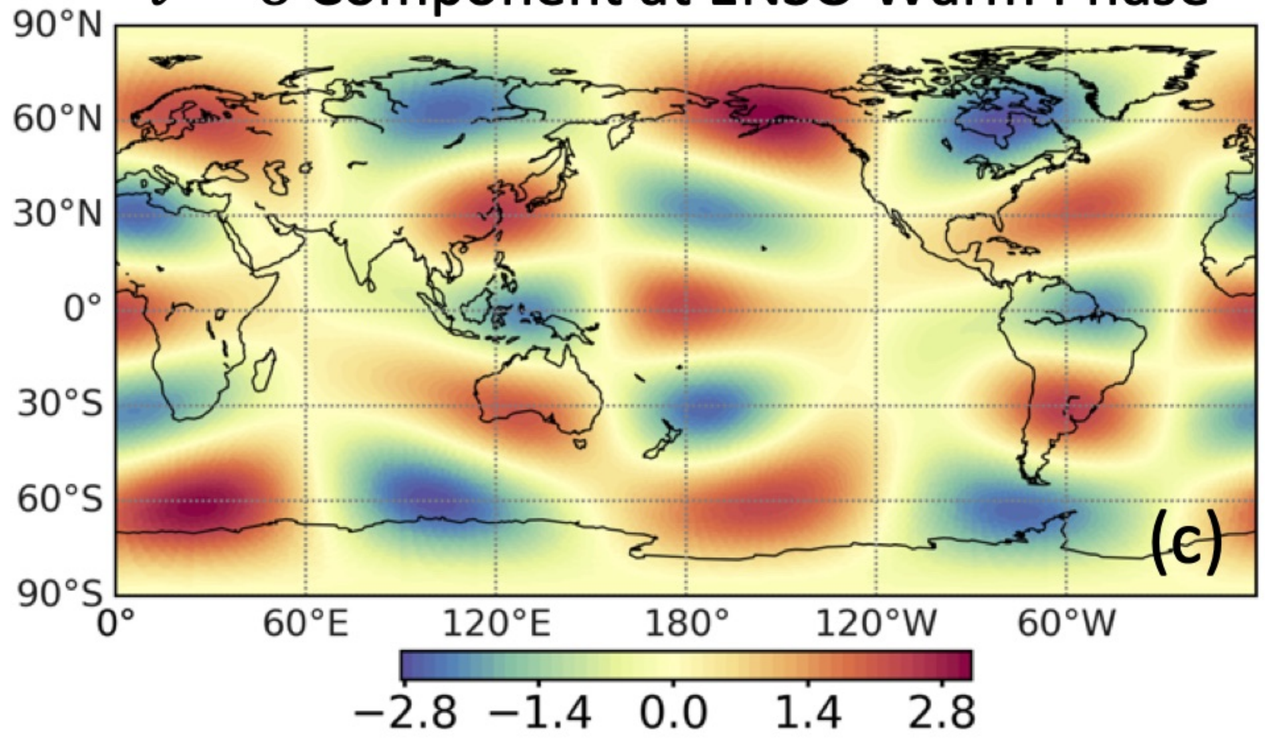
$l = 3$ Component at ENSO Warm Phase



$l = 3$ Component at ENSO Cold Phase



$l = 6$ Component at ENSO Warm Phase



$l = 6$ Component at ENSO Cold Phase

